

# Fine-resolution mapping of microforms of a boreal bog using aerial images and waveform-recording LiDAR

I. Korpela<sup>1</sup>, R. Haapanen<sup>1</sup>, A. Korrensalo<sup>2</sup>, E.-S. Tuittila<sup>2</sup>, T. Vesala<sup>3</sup>

<sup>1</sup>Department of Forest Sciences, University of Helsinki, Finland

<sup>2</sup>School of Forest Sciences, University of Eastern Finland, Joensuu, Finland

<sup>3</sup>Department of Physics, University of Helsinki, Finland

---

## SUMMARY

Boreal bogs are important stores and sinks of atmospheric carbon whose surfaces are characterised by vegetation microforms. Efficient methods for monitoring their vegetation are needed because changes in vegetation composition lead to alteration in their function such as carbon gas exchange with the atmosphere. We investigated how airborne image and waveform-recording LiDAR data can be used for 3D mapping of microforms in an open bog which is a mosaic of pools, hummocks with a few stunted pines, hollows, intermediate surfaces and mud-bottom hollows. The proposed method operates on the bog surface, which is reconstructed using LiDAR. The vegetation was classified at 20 cm resolution. We hypothesised that LiDAR data describe surface topography, moisture and the presence and depth of field-layer vegetation and surface roughness; while multiple images capture the colours and texture of the vegetation, which are influenced by directional reflectance effects. We conclude that geometric LiDAR features are efficient predictors of microforms. LiDAR intensity and echo width were specific to moisture and surface roughness, respectively. Directional reflectance constituted 4–34 % of the variance in images and its form was linked to the presence of the field layer. Microform-specific directional reflectance patterns were deemed to be of marginal value in enhancing the classification, and RGB image features were inferior to LiDAR variables. Sensor fusion is an attractive option for fine-scale mapping of these habitats. We discuss the task and propose options for improving the methodology.

**KEY WORDS:** airborne laser scanning, bi-directional reflectance, multi-image, peatland remote sensing, spatial variability, vegetation, 3D sensor fusion

---

## INTRODUCTION

Peatlands cover significant proportions of the Northern Boreal Zone, i.e. Fennoscandia, Canada, and Russia (Gorham 1991). They interact dynamically with the atmosphere through greenhouse gas exchange and currently have a net cooling effect on climate (Frolking & Roulet 2007, Gallego-Sala *et al.* 2018). In Finland, large-scale morphological characteristics distinguish the raised bog peatlands in the south from the northern aapa mires. Bogs exhibit small-scale (even sub-metre) topological complexity where drier hummocks, intermediate lawns, and wet hollows and pools vary along a water-level gradient (Figure 1). These microtopographical formations support different vegetation communities that have adapted to the prevailing moisture conditions. They differ also in their carbon gas dynamics: wetter surfaces are associated with higher CO<sub>2</sub> binding and CH<sub>4</sub> emissions than drier surfaces with lower decomposition rates (Maanavilja *et al.* 2011). In

general, northern peatland ecosystems are sensitive to changes in climate and the associated changes in hydrology (Ise *et al.* 2008). Peatland surface types are likely to respond differently to these changes (Strack 2008). Eutrophication can have similar effects, caused e.g. by air pollutants from local or distant sources. Historically, warmer and drier periods have led to an increase in hummock vegetation coverage at the cost of hollow vegetation (Väliranta *et al.* 2007). Consequently, climate change is likely to affect peatland carbon dynamics through changes in vegetation and especially through changes in the relative abundance of different surface types. Finding accurate and workable methods for monitoring bog microtopography and vegetation is important to augment our understanding of the phenomena outlined above. An efficient sampling scheme that applies accurately positioned and re-visited field plots constitutes an obvious choice. However, affordable point-based sampling does not capture spatial variation in the surroundings, which may be important for understanding and upscaling point-

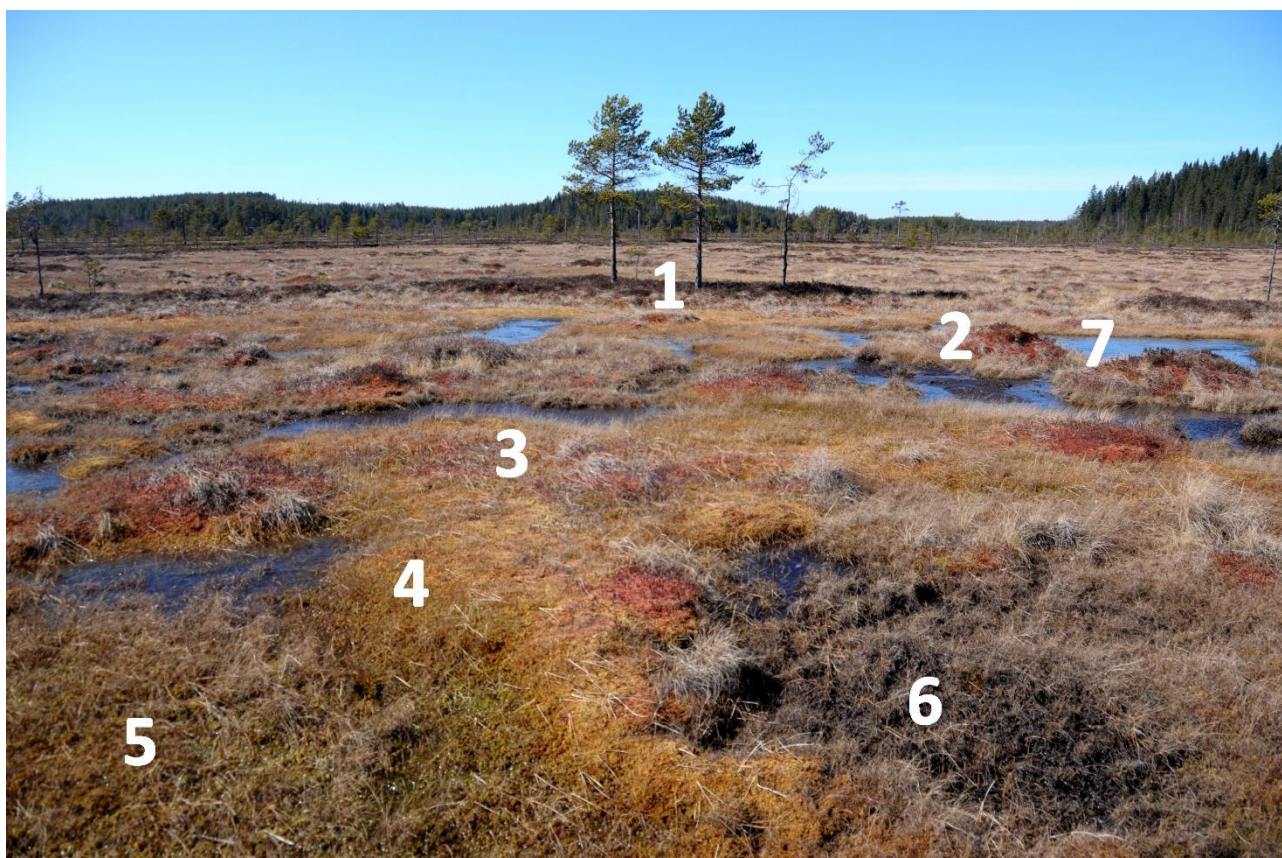


Figure 1. A close-range view of the study area with outlined vegetation classes: 1 = high hummock (HHU) ridge with 1–6-m high pine trees; 2 = hummock (HU); 3 = high lawn (HL) with reddish *Sphagnum rubellum*; 4 = lawn (L); 5 = hollow (HO); 6 = mud-bottom hollow (MB) with *Rhynchospora alba*; 7 = water (W). Cottongrass (CG) tussocks are pale-greyish in colour.

based observations and downscaling micro-meteorological eddy covariance (EC) fluxes (Morin *et al.* 2017).

This study was initiated by a request to provide ecosystem modellers with a detailed wall-to-wall map of vegetation near a station (Siikaneva II) measuring ecosystem-atmosphere relations on a bog (ombrotrophic mire) in southern Finland. The area comprises a mosaic of pools, wet hollows and mud-bottom hollows along with different lawn and hummock microforms (Figure 1). Previous systematic field surveys had proven very laborious due to poor accessibility, and resulted in geometrically distorted maps with sparse sampling. Thus, remote sensing became an obvious choice. The task resembles a case in Patagonia where Lehmann *et al.* (2016) used colour-infrared aerial images to map the microforms on an oroboreal bog.

### LiDAR and aerial imaging

Earlier studies showed that airborne discrete-return LiDAR intensity correlated with surface wetness, and hummocks and hollows on open and sparsely

forested mires were discernible in low-pulse density LiDAR data (Korpela *et al.* 2009). Airborne LiDAR, or laser scanning, is particularly suited for probing the geometry of forest canopies and the underlying terrain. The transmitted 2–10 nanosecond long laser pulse scatters from the illuminated targets and a portion of the returning photon surge is captured by the sensor, which measures (digitises) the profile of the returning signal and does range measurements on the fly (discrete-return system), or stores the ‘time-stamped’ waveform (WF) for post processing. The position and orientation of the moving sensor are known so that the distance measurement turns into 3D coordinates of the scattering scene elements. State-of-the art sensors process over a million pulses per second, sample the returning waveform at 1 nanosecond intervals, and detect very weak signals.

Siikaneva II is an open bog, where *Sphagnum* mosses prevail and stunted trees are rare. Thus, both occlusion and shading by trees are absent, permitting ‘radiometrically intact’ interpretation where LiDAR and image observations ‘meet on the bog surface’ (Figure 2). ‘Radiometrically intact’ means that the

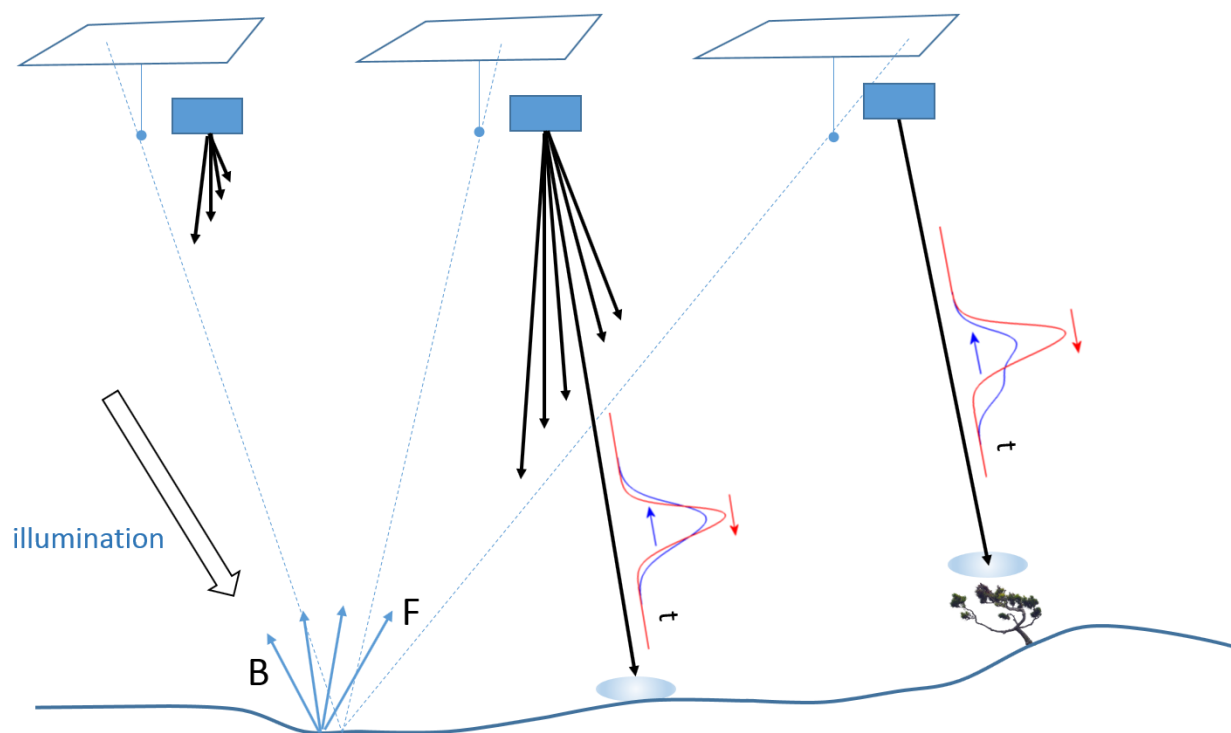


Figure 2. Illustration of ‘sensor fusion on the bog surface’. Airborne camera and LiDAR are operated concurrently such that the same surface patch is seen in several images (exposed at short intervals) and is sampled densely by LiDAR. The return waveform (blue) preserves its shape when sampling well-defined surfaces, while a tilted or rough surface or volumetric vegetation extends it. When the camera is moving, image observations are influenced by directional reflectance properties of the targets as the view direction (camera-target ray) changes. B = backscattering, F = forward-scattering geometry.

solar or LiDAR illumination of the surface targets is predictable, and the signal measured by a pixel or the LiDAR receiver depends mainly on the reflectance properties of the targets. While an image provides ‘continuous’ sampling of the scene, LiDAR pulses illuminate the scene pointwise and the sampling density and point pattern depend, for example, on the speed of the aircraft and the pulse frequency. The illuminated area is called a footprint and the irradiance in the cross-section of the footprint is Gaussian, as is the weight function of a pixel. The footprints are typically 10–40 cm in diameter from scanning distances of 0.5–3 km, while the field-of-view of pixels is narrower. Camera and LiDAR use different light sources, and whereas the illumination and view directions are coincided in LiDAR, they vary within an image and between images (Figure 2) because of the mutual geometry of the direct illumination and the camera-target ray changes.

Regarding the scale we note that our task of providing a map at 20 cm resolution differed from mire habitat classification, where the size of the habitats can reach several hectares and the characteristic patterns occur at multiple scales

(Vasander & Laine 2008, Korpela *et al.* 2009, Millard & Richardson 2013, Rapinel *et al.* 2015). National monitoring efforts using satellite images operate at the largest scale (e.g. Poulin *et al.* 2002, Haapanen & Tokola 2007).

#### Detailed hypotheses and summary of objectives

The microforms are associated with the water level and several microform types can occur within a distance of one metre, or a microform may extend for tens of metres (Figure 1). Each microform has characteristic vegetation. However, many species occur on more than one microform (Table 1). Hummocks are locally high and relatively dry, while the lower intermediate lawn, mud-bottom and hollow surfaces are wetter. Even centimetre-level changes show as variations in the flora and gas fluxes (Riutta *et al.* 2007). We hypothesised that detailed reconstruction of the microtopography would require high-density LiDAR and that field layer vegetation and/or surface roughness would influence the return LiDAR waveforms (WFs). Specifically, the return WF is a convolution of the transmitted pulse with the cross-section profile of the illuminated target, and the

Table 1. Mire surface types at Siikaneva II. The Cottongrass tussock (CG) class is not an original microform; it was added during the field campaign because it was clearly visible in the aerial images (cf. Kalacska *et al.* 2013).

Surface class (N)	Plant community description
High hummock, HHU (75)	High cover of dwarf shrubs ( <i>Empetrum nigrum</i> L., <i>Calluna vulgaris</i> (L.) Hull, and <i>Betula nana</i> L.). Bottom layer is dominated by <i>Sphagnum fuscum</i> (Schimp.) H. Klinggr.
Hummock, HU (118)	No shrubs, except for <i>Andromeda polifolia</i> L., which may constitute a significant percentage of the field layer. <i>S. fuscum</i> covers more than 10 % of the bottom layer.
High lawn, HL (89)	Field layer consists of <i>A. polifolia</i> and <i>Eriophorum vaginatum</i> L. Coverage of <i>S. fuscum</i> is less than 10 % and the dominant <i>Sphagnum</i> species is <i>S. rubellum</i> Wils.
Lawn, L (205)	Field layer may be missing, or scarcely covered by <i>Rhynchospora alba</i> (L.) Vahl., <i>Scheuchzeria palustris</i> L., <i>A. polifolia</i> , <i>E. vaginatum</i> or <i>Carex limosa</i> L. In the bottom layer, the dominant <i>Sphagnum</i> species are <i>S. papillosum</i> Lindb., <i>S. magellanicum</i> Brid. and <i>S. balticum</i> Russ.
Hollow, HO (169)	Field layer may be missing, or has <i>R. alba</i> , <i>S. palustris</i> or <i>C. limosa</i> . Dominant <i>Sphagnum</i> species are <i>S. majus</i> (Russow) C.E.O. Jensen and <i>S. cuspidatum</i> Ehrh. ex Hoffm.
Mud-bottom, MB (83)	Field layer may be missing, or scarcely covered by <i>R. alba</i> , <i>S. palustris</i> or <i>C. limosa</i> . Most of the bottom layer surface is covered by bare peat.
Water, W (-)	Open water surface without ground layer vegetation (pool). A few <i>S. palustris</i> shoots may be found.
Cottongrass, CG (17)	Tussock of <i>E. vaginatum</i> .

return WF extends (echo width) if the target is volumetric, tilted or non-planar. Furthermore, the low pine trees (0.5–5 m high) with sparse crowns should give rise to multimodal waveforms (Figure 2), which enables tree detection in LiDAR data. In addition, the return intensity is correlated with surface wetness. We note that the surface geometry could also be established using photogrammetric techniques. For example, Kalacska *et al.* (2013) used a ‘drone’ (UAV) with an RGB sensor to create an 11-hectare 2D image mosaic and thus locate cottongrass tussocks on a bog in Ontario, Canada.

Spatial dependencies are present in bog vegetation communities. For example, it is less likely for a tall hummock to be surrounded by open water than by high-lawn vegetation. Neighbourhood rules can enhance target classification (e.g. Niemeyer *et al.* 2013), but we omitted this approach because of lack of resources to collect the necessary field data and instead analysed the final results to assess whether they matched experience gained in the field in terms of neighbourhood relations.

The *Sphagnum* mosses that dominate bogs differ and vary greatly in colour, but no spectral reflectance data were available to support image interpretation. Because of budget limits, we used an RGB-sensor that was integrated with the LiDAR. Therefore, the research questions regarding image data were simple.

However, since occlusion and shading by trees is minimal on an open bog, we investigated how the images were influenced by directional reflectance effects, i.e. by the varying view-illumination geometry inside images and in overlapping images. This property can be regarded as a nuisance or exploited if multiple views are available - although real applications for directional reflectance anisotropy are very few (Korpela *et al.* 2014).

Our objectives can be summarised as follows:

1. Establish an accurate 3D match between field, image and LiDAR data to enable reliable 3D interpretation and testing of the hypotheses.
2. Find and analyse geometric and radiometric features to be used as predictors of the microforms. Examine particularly the gain from using the WF and multi-image data, and analyse directional signal patterns in images to see if they differ between microforms.
3. Test parametric and non-parametric classifiers in establishing the microform map in 20-cm resolution by applying an expert and a data-driven approach to feature selection. Carry out an elaborate accuracy assessment of the maps.
4. Generalise the experience gained and evaluate the applicability of the proposed methodology.

## METHODS

### Workflow of the study

Figure 3 shows the flowchart from data acquisition to the final classification. Tasks that ensured sufficient geometric and radiometric quality for hypothesis testing are highlighted. The data used are depicted by five grey rectangles. Airborne acquisitions were done in 2013 and fieldwork in 2012–2014. Changes in the vegetation were slow but it is likely that phenology, surface elevation, water level and surface wetness varied during this time. The remote sensing data were adjusted for deficiencies found in quality control. LiDAR WFs were corrected for system-induced effects ('FWHM calibration') because the receiver's response to strong signals caused a trend in echo width that was not related to surface roughness but was an artefact. The geometry of the aerial images was adjusted for a mismatch between flight lines and

a bias in focal length ('Augmented triangulation' in Figure 3). These steps aligned the image, LiDAR and field samples at an accuracy of better than 5 cm.

The flowchart shows two types of field observations. The 'GNSS positioned vegetation samples' ( $n = 756$ ) were georeferenced accurately and were used for pixel-by-pixel training and validation of the microform maps, while 'systematic surveys' were used for validation of the total distribution statistics as well as for the ordinate analyses of vegetation composition (Figure 4), diversity and overlap among the microforms. 'Close-range images' were taken for visualisation and their orientation was solved using scene elements that could be identified in the airborne data. Feature extraction, analyses and selection were carried out with the quality-controlled data. The selected features were then used as predictors by applying three different classifiers to create microform maps.

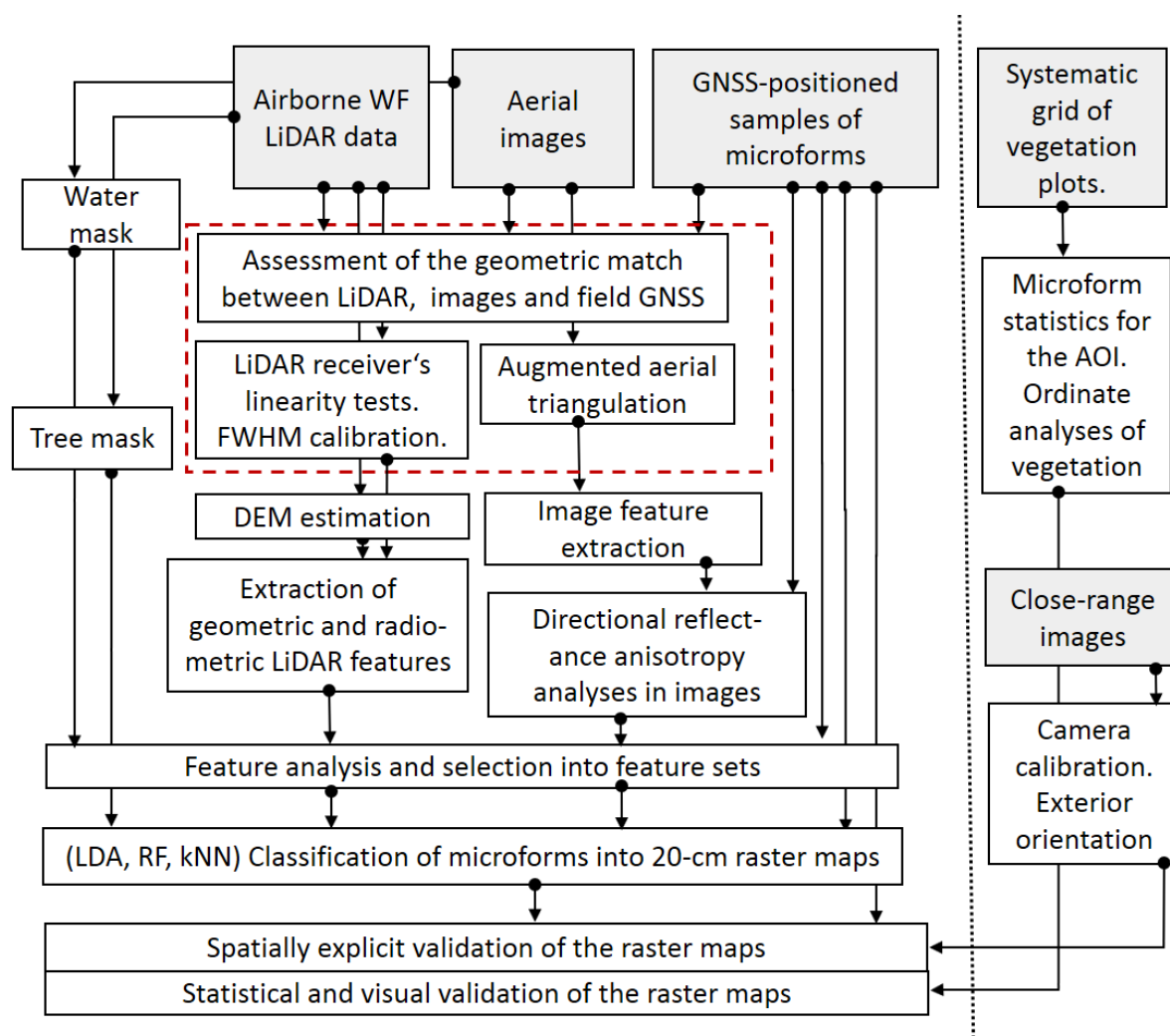


Figure 3. Flowchart of this study. The primary data and processing steps are shown to the left of the dotted line, while the data that were used for visualisation and spatially implicit validation are to the right. The red dashed rectangle identifies additional tasks that ensured data quality. See text for further explanation.

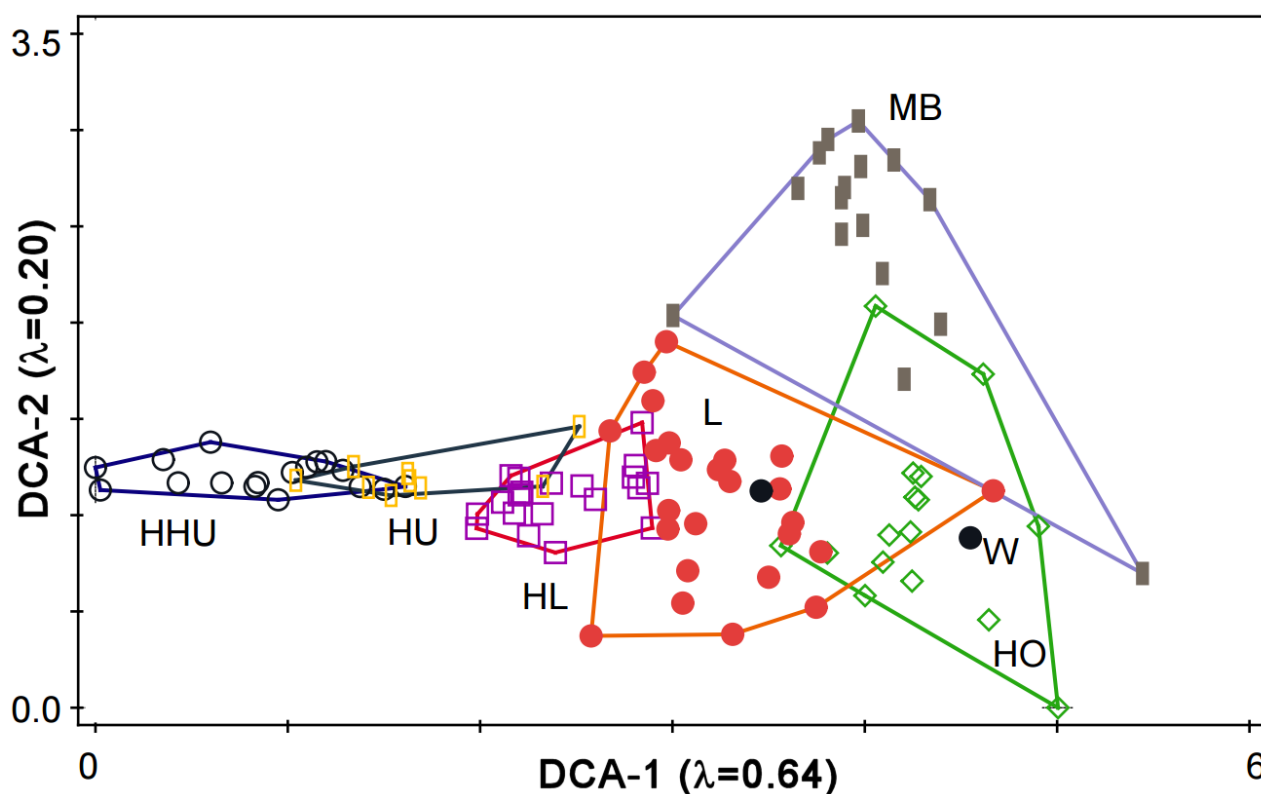


Figure 4. DCA results on plant community composition based on vegetation data collected in 2013. Sample plots that were classified into the same surface types in the field are enveloped together.

### Research site and field data

The site is a raised bog within the Siikaneva peatland complex in Finland, which is mainly dominated by aapa mires (Mathijssen *et al.* 2016; Figures 5, 6). The 16-ha area of interest (AOI) surrounds the Siikaneva II research facilities for monitoring energy, water and gas fluxes. Vegetation was surveyed in 2012 and 2013 using circular relevés, 30 cm in diameter. These data lacked accurate geolocations and we used them to validate the classified map as well as in ordinate analyses of the vegetation composition using detrended correspondence analysis (DCA; Figure 4) (Canoco 5.02, ter Braak & Šmilauer 2012). The projection coverage of each species, along with a microform class (Table 1, Table 2), was determined for the plant assembly. This classification captures the spatial variation in carbon dioxide and methane fluxes (Laine *et al.* 2007a, 2007b).

To provide accurately positioned field data for remote sensing, a field survey was done in April 2014 (Figure 6). The timing was optimal for accessibility, because the peat was frozen below the surface. Because of time constraints, sampling was in part subjective, i.e., not all locations had the same inclusion probability. Randomisation was secured by taking a certain number of steps to reach a sample. The samples ( $n = 756$ ) were circles of varying radius

(10–110 cm, representative of the sampled microform). Species in the moss and field layers (dwarf shrubs and herbaceous plants) were separately listed in order of coverage (Table 2) using the attributes ‘abundant’ and ‘sparse’ when necessary. We use Hämet-Ahti *et al.* (1998) for vascular plants and Laine *et al.* (2011, 2016) for mosses; the latter does not separate *S. magellanicum* into two species (cf. Hassel *et al.* 2018). The centre was GNSS-positioned at an accuracy of better than 3 cm.

### Aerial images

Imaging from a helicopter was concurrent with LiDAR acquisition (Table 3). Motion blur was observed in many of the images. The camera has a CCD array with wide spectral response functions of the Bayer-filtered pixels: 380–550 nm for blue (BLU), 450–620 nm for green (GRN) and 570– nm for red (RED). The specifications defined an accuracy that is better than 5 % for constant illumination across the CCD. No data were available for the stability of the shutter, i.e. variation of true exposure times. All images had the same nominal settings for aperture and exposure. The lens had distortions (deviation from a pinhole camera), which were compensated for using calibration coefficients that were reported in a camera calibration document.



Figure 5. A 200×200-m aerial image from May 2013. The EC tower is in the centre (350999.7E, 6859303.5N in UTM35). The darkest surfaces are water (W). Greyish surfaces are mud-bottom hollows (MB). The shadows of 1–5-m-high pines are barely visible on the ridge hummocks. Green-yellowish depicts hollow (HO) and lawn (L) surfaces (Table 1). The sub-image on the right shows an area of 19×28 metres.

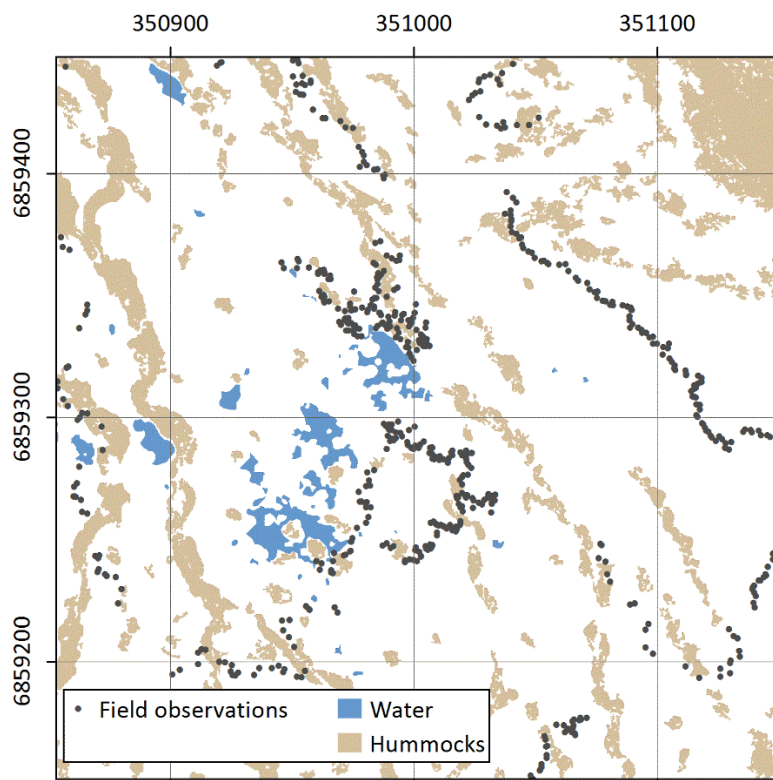


Figure 6. Map of the 756 vegetation plots of 2014.

Table 2. Moss and field layer species occurring in the samples of 2014. N is the number of plots on which the species occurred (was dominant). P shows the microforms where the species was present.

Species (abbreviation)	N	P
<i>S. fuscum</i> ( <i>Fus</i> )	180 (126)	HHU, HU, HL, L
<i>S. rubellum</i> ( <i>Rub</i> )	231 (116)	HHU, HU, HL, L HO
<i>S. angustifolium</i>	13 (5)	HHU, HU, HL
<i>S. papillosum</i> ( <i>Pap</i> )	150 (114)	HU, HL, L, HO
<i>S. cuspidatum</i> ( <i>Cus</i> )	117 (75)	HU, L, HO, MB
<i>S. majus</i> ( <i>Maj</i> )	89 (74)	L, HO
<i>S. balticum</i> ( <i>Bal</i> )	175 (69)	HU, HL, L, HO
<i>S. tenellum</i>	1 (1)	HL
<i>S. magellanicum</i> ( <i>Mag</i> )	47 (28)	L, HO
<i>S. lindbergii</i>	6 (6)	L, HO
<i>Polytrichum</i> sp.	1 (1)	HHU
<i>Dicranum</i> sp.	2 (2)	HHU
Lichen	4 (4)	HHU, HU
Mud	80 (80)	MB
Field layer		
<i>A. polifolia</i> ( <i>And</i> )	111	HHU, HU, HL, L HO, MB
<i>E. nigrum</i>	8	HHU, HU
<i>C. vulgaris</i> ( <i>Cal</i> )	51 (11)	HHU, HU, HL
<i>C. limosa</i>	44	HU, L, HO, MB
<i>R. alba</i> ( <i>Rhyn</i> )	274 (5)	HU, HL, L, HO MB
<i>E. vaginatum</i> ( <i>Erio</i> )	221 (27)	HHU, HU, HL, L HO, CG
<i>T. cespitosum</i>	26 (4)	HU, HL, L, HO
<i>S. palustris</i>	107	HU, HL, L, HO MB
<i>V. oxycoccus</i>	356	HHU, HU, HL, L HO

Table 3. Sensor and acquisition parameters for the airborne image and LiDAR data.

Camera	Hasselblad H4D
Date and time	28 May 2013; 11:30–11:50 GMT
Azim; Elev.	212.3° and 46.6°
Pixel size	6 × 6 µm, 4.5 cm
Bands	RGB, Bayer filter, 8 bits
Flying height	250–286 m AGL
Image size	6132×8176, 280×372 m
Focal length	3.5 cm
Overlap	68 % / 68 %
Spacing	88 / 120 m
F; exposure	f/6.8; 6.25 ms
Speed	35 m s <sup>-1</sup>
Flight lines	3 + 1
LiDAR	Riegl LMS-Q680i
Wavelength	1550 nm
Pulse Repetition Freq.	267 kHz
Scan angle	± 30°
Pulse density	47–81 pulses m <sup>-2</sup>
Divergence/footprint, 1/e <sup>2</sup>	0.3 mrad / 9 cm
WF sampling	1 ns at 8 bits
Width, FWHM	4.5 ns

### Geometric match of the image data and field data

The exterior orientation of the images (by the supplier, using MATCH-AT, Inpho, Germany) was deemed unsatisfactory as flight lines matched at an RMS accuracy of two pixels only. Therefore, we measured new tie points (using iWitnessPRO V4.0, Photometrix, Australia) and applied a later camera calibration in triangulation (bundle block adjustment, in-house software written in C++), which improved the RMSE to 0.6 pixels (3 cm). When the XYZ coordinates of the tie points were contrasted with LiDAR and field GNSS, a consistent 30-cm vertical offset was observed, and it was compensated by correcting the camera constant by 0.1 %. Planimetric XY accuracy was analysed by letting the bright cottongrass and dark mud-bottom samples vary systematically around their GNSS positions. The samples were small and distinct (cf. Kalacska *et al.* 2013). The brightness features peaked consistently at offsets of less than 5 cm, i.e. the images matched well in 3D with the field GNSS.

### Properties of the WF-recording LiDAR data

The LMS-Q680i WF-recording sensor (Table 3) transmits 4.5-ns-long pulses, which have a bell shape in the time domain. The return pulse is a convolution of the transmitted pulse with the backscatter cross-section profile of the illuminated targets. Backscatter cross-section corresponds to backscatter reflectance in well-defined planar targets such as *Sphagnum* surfaces, in which the return pulse preserves the shape of the system WF and the peak amplitude can be used as a proxy for reflectance. However, if the pulse arrives at an oblique angle, the return WF is extended and the peak is dampened, which can be difficult to correct for in real data (Jutzi & Gross 2009, Kaasalainen *et al.* 2011). This effect was expected to remain below 0.2 ns (3 cm) in our data, because the scan zenith angles varied from 0° to 30° and the pulses were 9 cm in diameter. The return pulse widens also if the backscatter cross-section profile extends over a depth (Figure 2), which is typical in vegetation (Höfle & Pfeifer 2007, Wagner *et al.* 2007). For example, a pulse that reflects from two surfaces that are separated by 30 cm widens by two nanoseconds. The widening thus relates to surface roughness, which we wanted to exploit (cf. Doneus *et al.* 2008). The sensor digitised the amplitude values of the return signal at 1 ns intervals. The storage was limited to meaningful 60-sample sequences, between which the storage could be stopped, which may result in missing sequences of very low backscattering between tree canopy and the ground (cf. Korpela 2017). Completely missing data was observed in Siikaneva for pulses that were

entirely absorbed by water.

LMS-Q680i hosts two receivers that follow a common photon detector. This detail became relevant because the so-called high-gain receiver's WF data were saturated for the strongest signals. The saturation caused the calculated full-width-at-half-maximum (FWHM, echo width) to depend on target brightness, which was undesirable as we sought pure measurements of surface roughness. Echo width of planar targets increased with increasing peak amplitude, from 4.4 to 5.0 ns, although it should not change at all. We corrected this using a model that predicts the FWHM of well-defined targets by accounting for the influence of signal strength. The ECHOW feature was defined as a deviation from this baseline, i.e. if the observed FWHM was 6.0 ns for a strong signal, ECHOW was 1.0 ns.

In addition to WF data, we had discrete returns (XYZ points with return intensity), which were postprocessed to provide ratio-scale intensity values. Owing to ratio-scale data, we could normalise the intensities for range-dependent spherical losses (Ahokas *et al.* 2006, Korpela 2008). This reduced intensity variation, which is up to  $\pm 30\%$  in well-defined surfaces at scan zenith angles reaching 30 degrees. We note that the correction of spherical losses is ambiguous in canopies (Korpela *et al.* 2010, Gatzliolis 2011, Korpela 2017), but we used intensity data for the bog surface only.

### Geometric match between LiDAR and field data

The LiDAR echoes were processed into a raster elevation model (DEM) at 10 cm resolution. Validation showed an RMSE (including 2–3-cm imprecision of the 756 GNSS points) of 4.2 cm and a mean error of +0.3 cm. The inaccuracy of high hummock (HHU) was largest, while high lawn (HL) showed the smallest errors. The match between LiDAR and GNSS was analysed, as for the images, by letting the GNSS positioned samples move. The RMS of differences reached a minimum of 4 cm at a 2-cm XY offset, which implied high accuracy of co-registration.

### Derivation of LiDAR-based features for microform classification

Table 4 lists the features computed from the DEM and Figure 7 illustrates three important LiDAR-based features. INTENSITY was based on the intensity values of single-echo pulses with ECHOW < 6 ns and height < 0.5 m (ground echoes free from canopy transmission losses). A binary WATER mask was delineated manually using several aerial images in the digitisation. A binary TREE mask was based on echoes with a height > 0.6 m.

### Image feature extraction

The RGB values for the 3D surface points were retrieved using standard collinear equations and the values in each image were collected from an  $N \times N$  window, where  $N$  was tried at 1, 3, 5, 7 and 9. The image features included the mean, the standard deviation, the maximum, the minimum, and the 25 % and 75 % quantiles of the RED, GRN and BLU bands as well as the band ratios and the first principal component.

### View-illumination geometry and variance analysis of image data

We investigated directional signal anisotropy in images. If microforms display similar anisotropy, this enables the use of a single correction of the image values to nadir geometry at  $(x=0, y=0)$  in Equation 1. Between-class differences would potentially enable exploitation of the anisotropy in classification, although real applications are few (Korpela *et al.* 2014). In brief, each image observation is made from a view direction and the target is mainly illuminated from one direction. These vectors are collinear in LiDAR, while their mutual geometry varies from image to image. We modelled the directional anisotropy by assuming a fixed illumination, as imaging lasted only

20 minutes. The geometry was thus simplified to azimuth difference ( $\phi$ ) and the view zenith angle ( $\theta$ ).  $\phi$  is the difference between the solar azimuth and the azimuth of the target-camera ray. It ranges from  $0^\circ$  to  $180^\circ$ . The range of  $\theta$  was defined by the field-of-view of the camera and was  $<40^\circ$ . A transformation into a polar representation followed:

$$x = \theta \cdot \cos(\phi); y = \theta \cdot \sin(\phi) \quad [1]$$

In nadir,  $x = 0$  and  $y = 0$ . For small values of  $y$ , the pixels are near the principal plane, where the camera, target and sun are aligned. Backscattering geometry is associated with positive values of  $x$ , while negative values denote forward-scattering geometry (Figure 2). Natural targets appear brighter in backscattering geometry because the shaded sides remain invisible, while the opposite is true in forward-scattering geometry. The directional effects are also influenced by the atmosphere, but we made no attempt to correct atmospheric effects, i.e. to derive reflectance quantities; thus, we apply the term 'signal'.

The anisotropy was investigated using regression analysis by fitting Equation 2 to the image features (cf. Korpela *et al.* 2011). The parameters were chosen using stepwise selection in both directions. Strong predictors were retained to avoid improbable oscillation.

Table 4. DEM features implemented in QGIS (Quantum GIS Development Team 2015), ArcGIS (ESRI Inc., Redlands, CA, USA), GRASS GIS (GRASS Development Team 2015), or on an in-house photogrammetric workstation.

Feature	Description
SDEV	Standard deviation in a $3 \times 3$ ( $30 \times 30$ -cm) window. Local surface roughness and/or slope.
SLOPE & SRANGE	QGIS 2.10: maximum rate of change in a $3 \times 3$ window. The range of slope values.
HU-IND	A 'hummock index' that looks for the minimum elevation up to a specified distance, in eight cardinal directions, and computes the difference.
DEPR-IND	A 'depression index'. Collects elevations from the eight cardinal directions up to a specified distance and fits univariate regression to each direction. Computes the sum of the coefficients, which are assigned +1 or -1 for positive or negative coefficients. A 'perfect peak' is 8, while -8 corresponds to a depression. Finds the small-scale variation in the mire surface.
FLATNESS	Computed in a window by taking the smallest sum of elevation differences among the eight cardinal directions. Indicates if the point of interest has a local flat surrounding in at least one of the directions.
DISTHUM	Distance to closest hummock border (HU-IND $> 0.2$ m). The thresholded HU-IND raster was processed twice with the majority filter in the Spatial Analyst of ArcGIS. Then, unique labels were given for each contiguous area. This raster was converted into vector format and areas smaller than $10 \text{ m}^2$ were removed. Finally, the Euclidean distance tool was applied to create a map with distances to the closest hummock.
Texture features	Textural features Contrast, Entropy, Angular Second Moment and Inverse Distance Measure were derived in GRASS. The features were computed in $3 \times 3$ and $5 \times 5$ neighbourhoods.

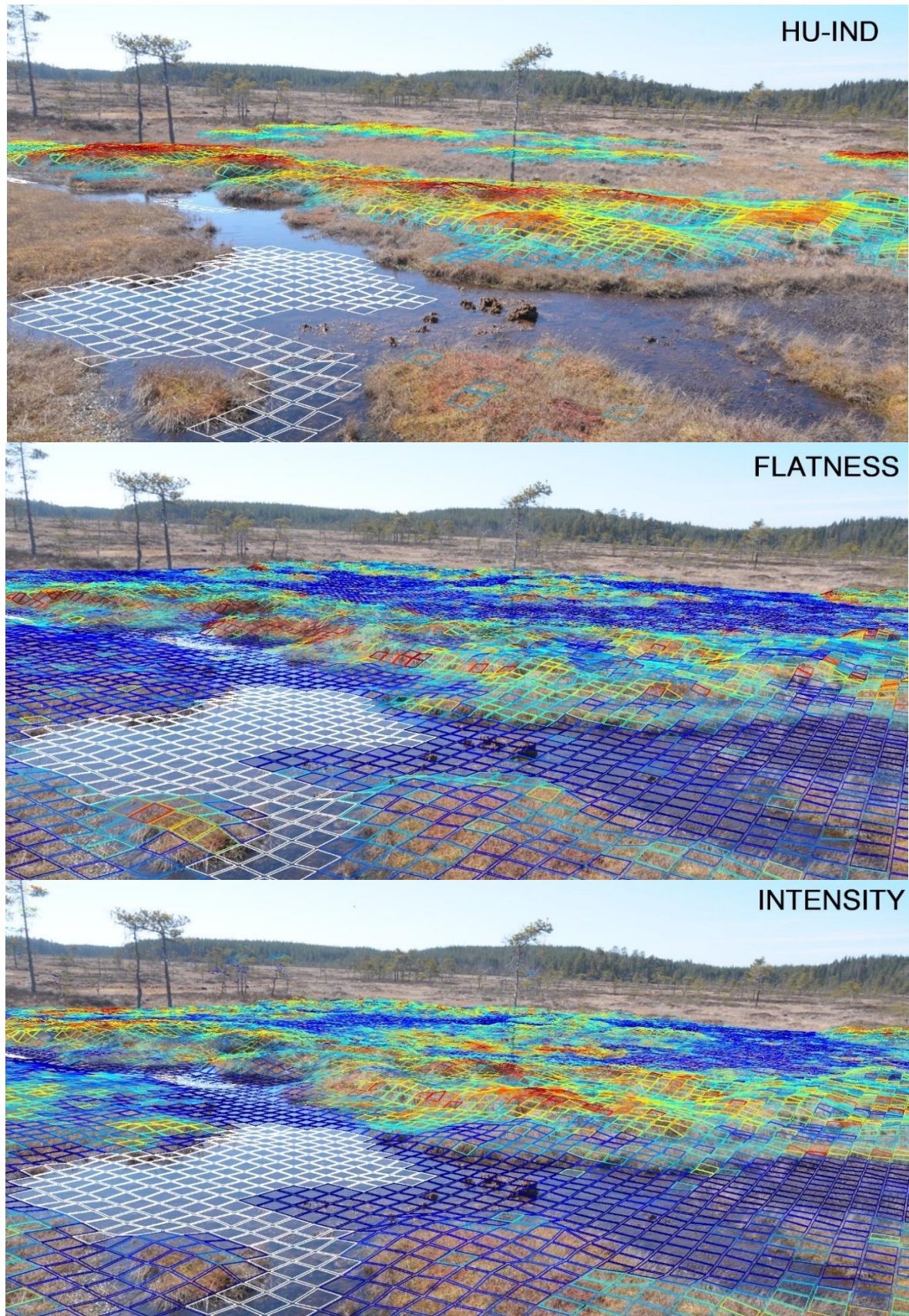


Figure 7. Illustration of the HU-IND (large values only), FLATNESS and INTENSITY feature maps. The white cells are WATER. FLATNESS peaks in slopes. INTENSITY is high in hummocks and low in water, hollows and mud-bottoms. The raster cells are  $20 \times 20$  cm.

$$DN(x,y) = a_0 + a_1x + a_2y + a_3xy + a_4x^2 + a_5y^2 + a_6x^2y + a_7xy^2 + a_8x^2y^2 + a_9x^3 + a_{10}y^3 + \varepsilon \quad [2]$$

In Equation 2, *DN* is the image feature for a mire surface patch that is seen in the given *xy* geometry. When Equation 2 was fitted, the mean values (*a*<sub>0</sub>) were obtained for the nadir geometry (Table 5).

We can assume that the variance of image observations representing a microform class is explained by directional anisotropy-trend (Equation 2, Figure 8), a sample effect and residual error. Mixed-effect models (Equation 3) were fitted to the data on each band and microform to analyse the sources of variance. The sample effect is supported by the idea that the species composition influences the observed ‘reflectance’ and causes the sample to appear ‘bright or dark’ in all geometries. Directional signal

Table 5. Mean image *DN* values at nadir and the corresponding band ratios .

	HHU	HU	HL	L	HO	MB	CG
RED	152	162	166	164	162	140	180
GRN	138	140	142	141	143	127	165
BLU	110	112	112	101	102	116	134
R/G	1.10	1.16	1.17	1.16	1.13	1.11	1.09
R/B	1.38	1.44	1.48	1.61	1.58	1.21	1.34
G/B	1.25	1.25	1.27	1.39	1.40	1.09	1.23

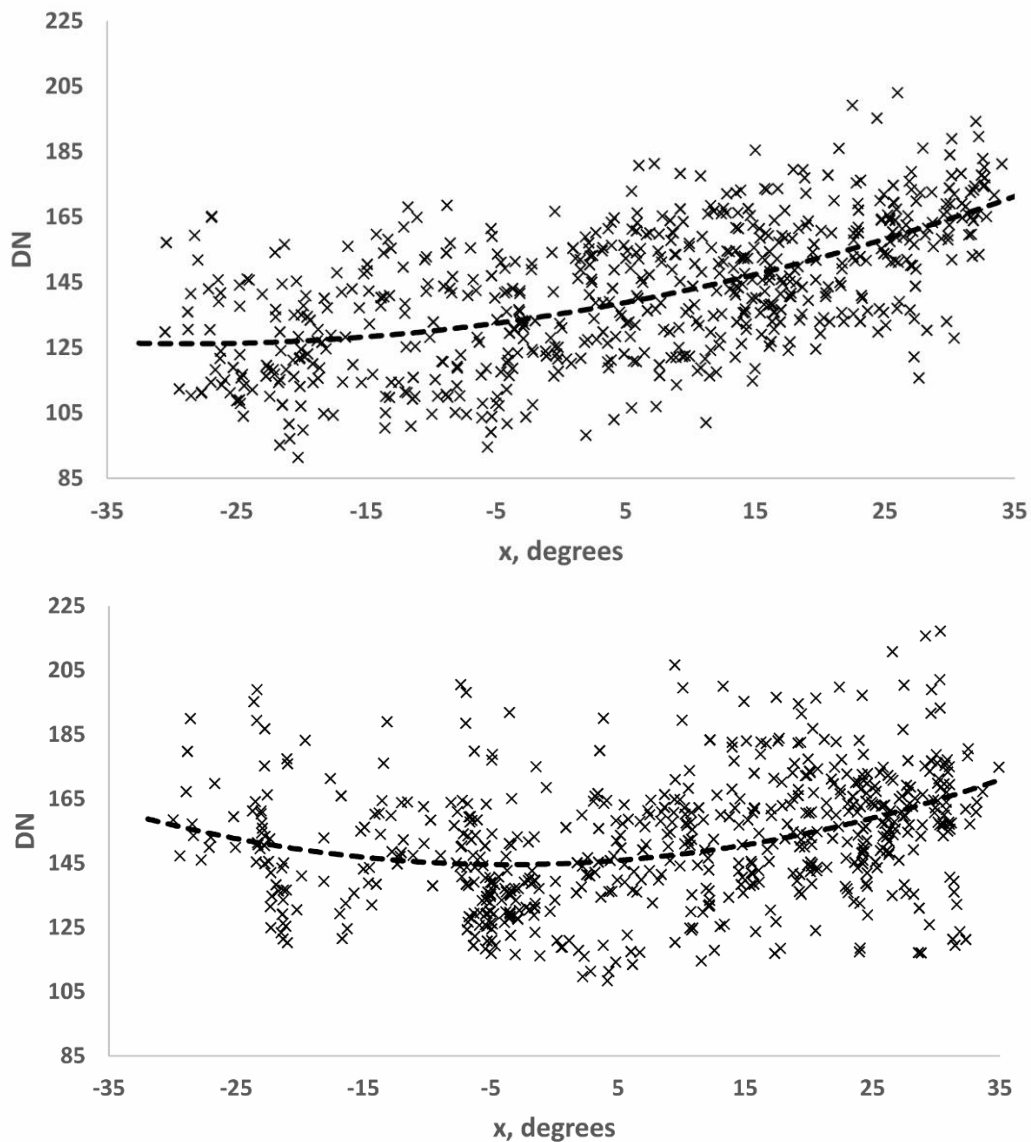


Figure 8. GRN band mean feature as a function of *x* in Equation 1. HO (upper pane) shows an increase also in the forward scattering geometry (*x* < 0°), while HHU (lower pane) shows a decrease.



anisotropy (the term  $DN(x,y)$  in Equation 3) explained 4–34 % of the variance, while the target effect explained 56–83 %, and the residual variance was 7–20 % (Table 6). In L, 83 % of the GRN band variance is due to the targets, i.e. a bright L sample is bright in all images. In lawn (L), the mix of *Sphagnum* species can vary greatly. Similarly, hollows (HO) are rather homogenous, but their colour varies from sample to sample according to the dominant *Sphagnum* species and wetness, and the target effect is strong (Table 6, Figure 9). Mud-bottom hollows (MB) display dark colours for the wet cases and are greyish when *R. alba* occurs. In high-hummock (HHU), anisotropy explains as much as 34 % of the BLU band variance. HHU, HU and CG are microforms where directionality explained 20 % or more. Their vegetation casts shadows and they remain unseen in the backscatter geometry. The residual variance cancels out when multiple images per target are available; the values were low.

$$DN_{class,band} = DN(x,y) + \text{sample effect} + \varepsilon \quad [3]$$

Directionality ( $DN(x,y)$ ) poorly explained the signal variance in surfaces lacking vascular plants (HL, L, HO, MB) and the weak trends showed an increase in both directions along the solar principal plane, while in shrub-rich HHU and HU the signal decreased slightly in the forward scattering direction (Figure 8). The results suggest that single band-specific directional anisotropy models (i.e. Equation 2 fitted to all data) will not be optimal for correcting the pixel values to common nadir geometry. This weighting is important if the image data are not balanced, i.e. if some areas are seen in only one geometry.

### Feature analyses and selection for microform classification

We first aimed to find predictors using expert judgment relying on experience in statistical feature

Table 6. Partition of DN (mean values in  $5 \times 5$  window) variance between the terms of the mixed-effects models (Equation 3). Percentages (%) of total variance.

Class	Anisotropy			Target			Residual		
	R	G	B	R	G	B	R	G	B
HHU	31	28	34	60	62	56	9	10	10
HU	20	13	17	61	75	69	19	12	14
HL	12	7	10	69	83	77	19	10	12
L	7	8	8	79	82	80	14	10	12
HO	5	12	8	83	73	81	12	15	11
MB	5	5	4	79	74	79	16	21	17
CG	25	17	25	67	74	68	8	9	7

selection and our knowledge about the mire vegetation and the data, to avoid a black-box approach. ANOVA, Tukey's test, correlation analyses and LDA (linear discriminant analysis) provided help in selecting the expert variables. The second approach was data-driven and used the feature importance metrics of the random forest (RF) algorithm.

### Classification methods

The classifiers included parametric and non-parametric methods: the  $k$ -nearest neighbour (kNN), LDA and RF (Breiman 2001, Hastie *et al.* 2001, Liaw & Wiener 2002). Maximum likelihood was applied in LDA to estimate the class means and covariances. Leave-one-out validation was used with kNN and LDA, whereas out-of-bag (OOB) validation was used with RF. Five nearest neighbours were searched for with kNN, and class determination was based on the

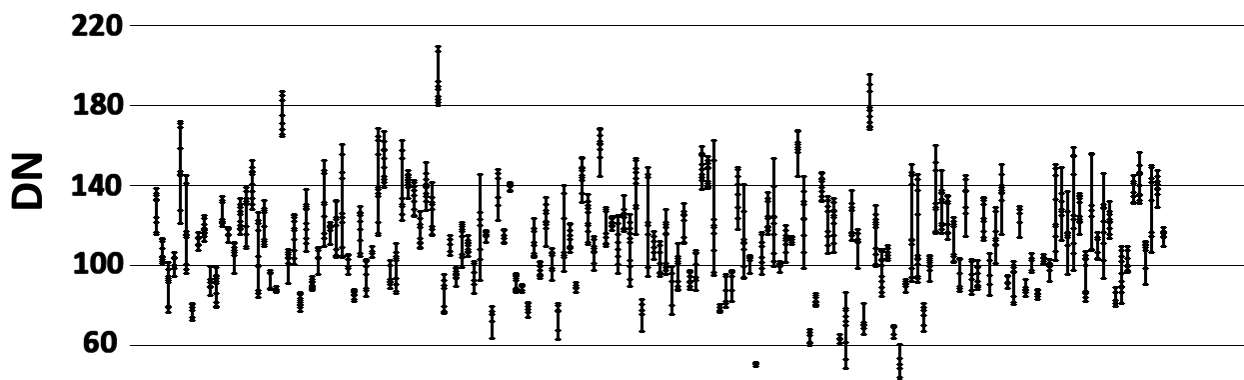


Figure 9. RED band values (5–12 images per sample) of HO sample plots. The vertical line joins the observations of images that 'view' the sample plot. The target effect for HO on RED band was 83 %, which is reflected by the clustering in the Figure.

inverse Euclidean distances. kNN features were standardised to zero-mean and unit-variance. A total of 350–500 trees were used in RF, which was based on the saturation of the OOB estimates.

## RESULTS

### Feature analysis for microform classification

Because of the anisotropy, the analyses were constrained by the view-illumination geometry. For example, Figure 10 shows that MB and CG separated well in the RED/GRN image feature. The influence of the *Sphagnum* species on image features was examined by species groups. The largest differences were observed in the band ratios. RED/GRN was the highest in reddish mosses - *S. magellanicum* and *S. rubellum* (Figure 11). The greenish *S. cuspidatum* showed the lowest RED/GRN values. HO surfaces have a low RED/GRN ratio, which is in line with findings concerning *S. cuspidatum* and *S. majus*. Concerning the field layer, the presence of *C. vulgaris*, *A. polifolia*, *E. vaginatum* or *R. alba* resulted in lower RED/GRN values (Figure 11) probably because of shadow-casting and 'greyish colours' of the listed species. It is evident that the motion blur caused an averaging effect that reduced the differences in Figure 11.

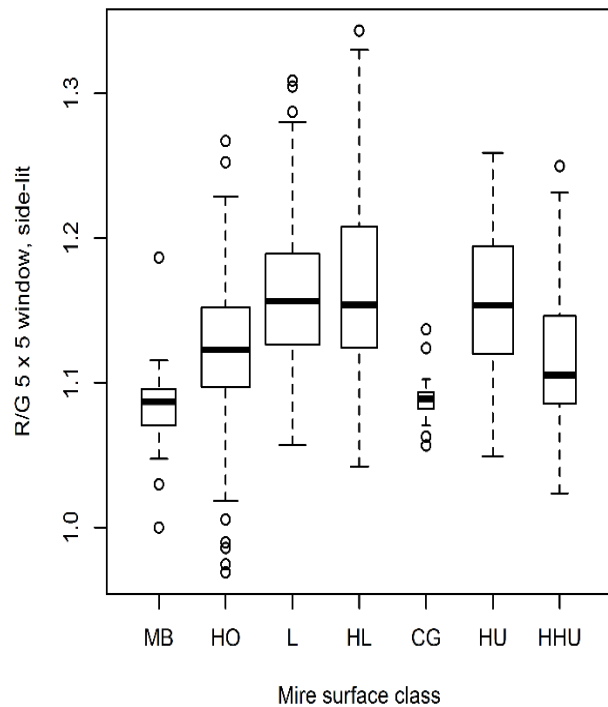


Figure 10. Boxplot diagram for the RED/GRN image feature. Observations are constrained by azimuth difference ( $45^\circ > \phi < 135^\circ$ ). The width of the bars depicts the number of observations.

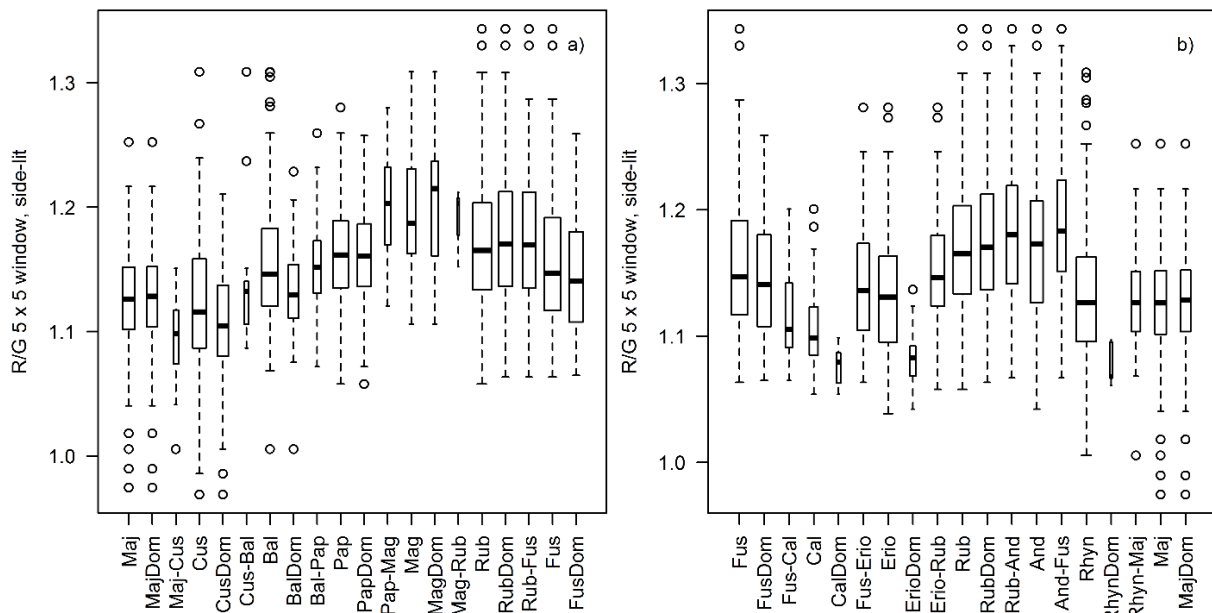


Figure 11. Boxplot comparison of the RED/GRN image feature in plots vegetated by (a) *Sphagnum* mosses only and (b) *Sphagnum* mosses with field layer vegetation. The labels 'XXX', 'XXXDom', 'XXX-YYY' are interpreted as 'Species XXX is found', 'Species XXX dominates' and 'Both XXX and YYY are found', respectively. Abbreviations are given in Table 2. Azimuth difference is limited to  $90^\circ \pm 45^\circ$  (stratum) to constrain the directional effects. Note that groups are not limited and, for example, *S. balticum* can occur in groups 'Maj', 'MajDom', 'Maj-Cus', etc.



The microforms exhibited characteristic traits in many LiDAR-based features. The hummock index (HU-IND) measures the height relative to local water level and showed a clear response from MB to HHU (Figures 7 and 12). The depression index was correlated with the hummock index but was specific in CG (data not shown). According to expectations, INTENSITY was lowest in wet surfaces (Figure 12). The variation was high in MB, probably because of ample within-class variation in wetness and the varying presence of field layer. CG was bright in both RGB and LiDAR. As could be expected, ECHOW differed in CG and HHU surfaces, owing to the vegetation and rough topography. The 0.1–0.4-nanosecond difference corresponds to a 1.5–6-cm depth variation (Figure 12). ECHOW varied the least in L and HO, which is reasonable as these surfaces are flat and have sparse field layer. ECHOW should rise with increasing scan zenith angle and the maximal widening should have been approximately 0.2 ns (3 cm) at the 32° oblique angle. However, the effect was not observable. Figure 13 shows the relationship of the *Sphagnum* species with local elevation. *S. fuscum* is a hummock species while *S. majus* and *S. cuspidatum* grow in hollows.

**Feature selection for microform classification**

As already explained, we aimed for deductive 'expert features' and data-driven 'RF features'. Selection was done for image and LiDAR features in addition to their combination. The best single-image features were the mean features of RED, GRN and BLU as well as the band ratios. The window size had only a minor effect. As each surface point in the 20-cm grid could be viewed in up to 14 separate images, we computed mean features by calculating the average of the single-image features, as well as by calculating the average of observations that were first normalised to the nadir geometry, using the *xy*-dependent parts of

the per-band anisotropy polynomials (Equation 2) that were estimated in data that combined all microforms. The band-ratio image features showed only very weak signal anisotropy.

HU-IND was always the best single LiDAR predictor (Figure 12, Tables 7 and 8). It measures local elevation and was an important RF variable for the detection of HO, HU and HHU. Similarly, the textural DEM features showed lower F-values than the simple standard deviation. The Gini-importance measure of RF was mostly in line with F-tests, except for DISTHUM, which was a more significant predictor in RF.

In Tukey's test, the mean RED and GRN/BLU image features were able to separate three classes,

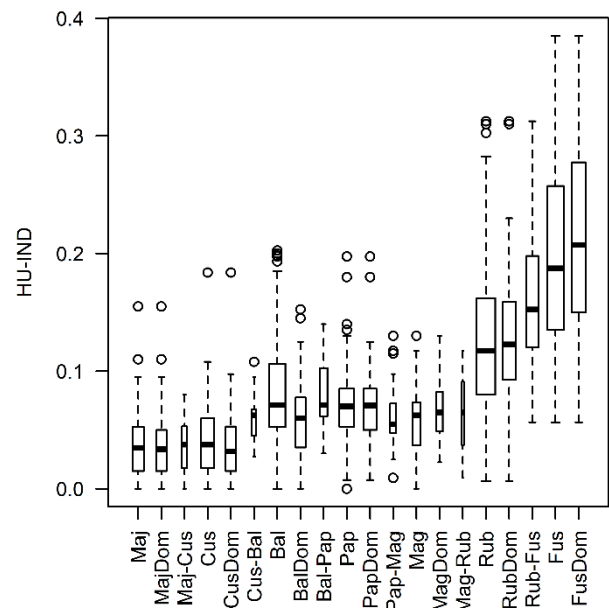


Figure 13. Boxplot of the hummock index (HU-IND) in vegetation plots, where *Sphagnum* moss species occurred in various combinations. See also Figure 11 for an interpretation of the classes.

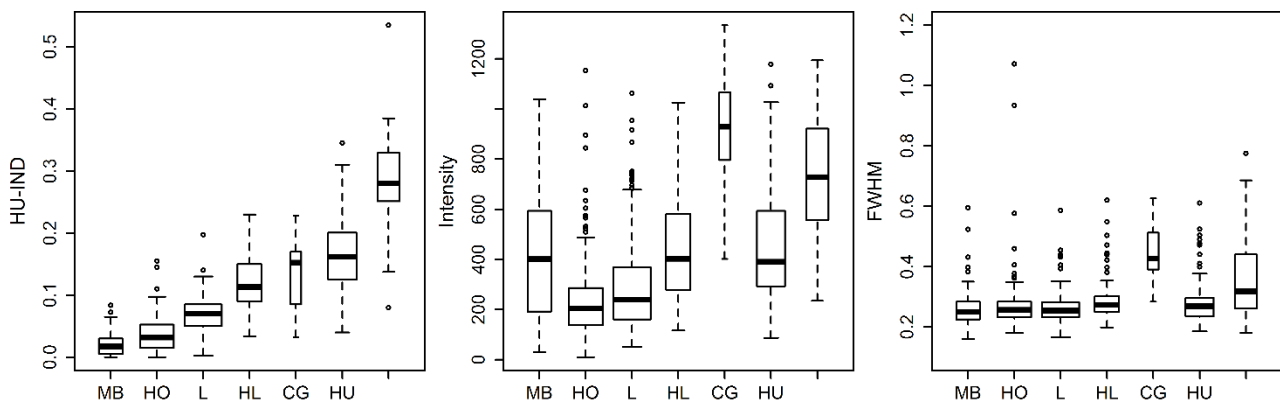


Figure 12. Boxplot graphs of three LiDAR features. FWHM refers to ECHOW feature.



whereas the other bands or band ratios could separate only two; or in the case of RED/GRN, none (not tabulated). The classes that differed systematically were CG (bright) and MB (dark), followed by HO. The best LiDAR descriptors were HU-IND and DEPR-IND, which were able to separate 5–6 of the seven classes. The separation of HO and MB as well as L and CG using image features was particularly advantageous (cf. Kalacska *et al.* 2013), as these classes separated poorly using the DEM features HU-IND and DEPR-IND.

Expert features combining both data sources were GRN, BLU, RED/GRN, HU-IND, SDEV, DISTHU

and INTENSITY. Expert LiDAR variables were HU-IND, SDEV, DISTHU, INTENSITY and DEPR-IND, while the expert image features included the mean features and the band ratios. The RF variables are shown in Table 8. Classes with the highest or lowest elevation ranked HU-IND as the most important variable, whereas the classification of intermediate classes HL and L benefited from image observations. RF-selected LiDAR features were HU-IND, DEPR-IND, INTENSITY, DISTHU, SDEV and SRANGE. The RF-selected image features had the mean R and G features, as well as the band ratios.

Table 7. F-values for some of the LiDAR-based features.

Feature	F-value
Hummock index (HU-IND)	420
Depression index (DEPR-IND)	133
Flatness index (FLATNESS)	38
Standard deviation of Z (SDEV)	54
Range of slope	37
Slope	20
Distance to nearest hummock (DISTHU)	4
Other features	
INTENSITY	77
ECHOW	11

Table 8. Twelve variables selected by RF (sensors combined).

Feature	Gini	Ranks highest for classes
HU-IND	121	HO, HU, HHU
G/B	83	HL, MB
DEPR-IND	62	
R/B	59	
R/G	55	L
INTENSITY	42	CG
DISTHU	38	
FLATNESS	36	
R	31	
G	30	
B	30	
ECHOW	30	

### Classification results and validation

Table 9 shows that LDA and RF performed quite similarly. The highest overall accuracy (OA), 71 %, was obtained with RF and the corresponding microform map is shown in Figure 14. The combined features outperformed the use of LiDAR or image features only. Class-by-class results in Figure 15 show that the accuracy of HL was low, 25–42 %.

The error matrices for LDA are in Table 10. High lawn (HL) was deemed variable in the field, and this was also displayed in the ordinate analyses (Figure 4). Because of the similarities in vegetation (e.g. the red *S. magellanicum* and *S. rubellum*) and elevation, HL was confused with lawn (L) and low hummocks (HU). Mud-bottom hollows (MB) were classified best and only a few hollow (HO), L and CG samples were misclassified into MB. L was misclassified into the 'neighbouring' classes HO and HL. It is worth noting is that L was the most common

Table 9. Best-case classification performance in leave-one-out and out-of-bag validation in overall accuracy and ( $\kappa$ , kappa statistic) using the three classifiers and two feature sets.

Feature set	Classification method		
	LDA	RF	kNN
Expert – Combined	69 (0.62)	67 (0.59)	62 (0.53)
RF – Combined	68 (0.60)	71 (0.64)	61 (0.52)
Expert – LiDAR	57 (0.46)	59 (0.49)	52 (0.41)
RF – LiDAR	57 (0.47)	61 (0.52)	50 (0.38)
Expert – image	54 (0.43)	52 (0.40)	49 (0.37)
RF – image	53 (0.43)	53 (0.42)	49 (0.38)

class in the field (Table 1). Many (30–39 %, Table 10) HO samples were classified as L, which had a significant effect on the overall accuracy, as HO was the second largest class. The 'better' performance of RF was due to an improved detection of the HO class (Figure 15). Figure 16 illustrates the classification results in a close-range image.

If we did not treat confusion between HU and HL, HL and L, L and HO as errors, OA increased to 79 % ( $\kappa = 0.74$ ) with LDA and to 85 % ( $\kappa = 0.76$ ) with RF.  $\kappa$  is the simple kappa statistic. Confining to samples having a radius  $>15$  cm ( $N = 626$ ),  $\kappa$  in RF improved from 0.64 to 0.66. Restricting the radius to  $>25$  cm,  $\kappa$  was 0.68. The improvements are explained by the small geometric imprecision that influences small samples. The general correction of image feature values to nadir-geometry reduced the OA by 1–1.5 % compared to the direct use of averages. This decrease

in accuracy is explained by the between-class differences in directional reflectance, and the nadir correction incorrectly weighted the image observations.

The results of the classification were contrasted with the field inventory data from 2012 (Table 11). The proportion of L was overestimated using remote sensing, while HL and HHU were underestimated. The spatial dependencies between microforms were analysed to further validate the microform map. The  $3 \times 3$ -neighbourhood analyses in Table 12 show, for example, that the tree mask-based tree crowns are compact (Tree-to-Tree connectivity is 93.8 %) and grow on HHU surfaces (4.7 %). Similarly, CG, HL and HU form small patches as their self-connectivity values are low. These findings are rational, as is the result indicating that the most common neighbours of water patches are MB, HO and L.

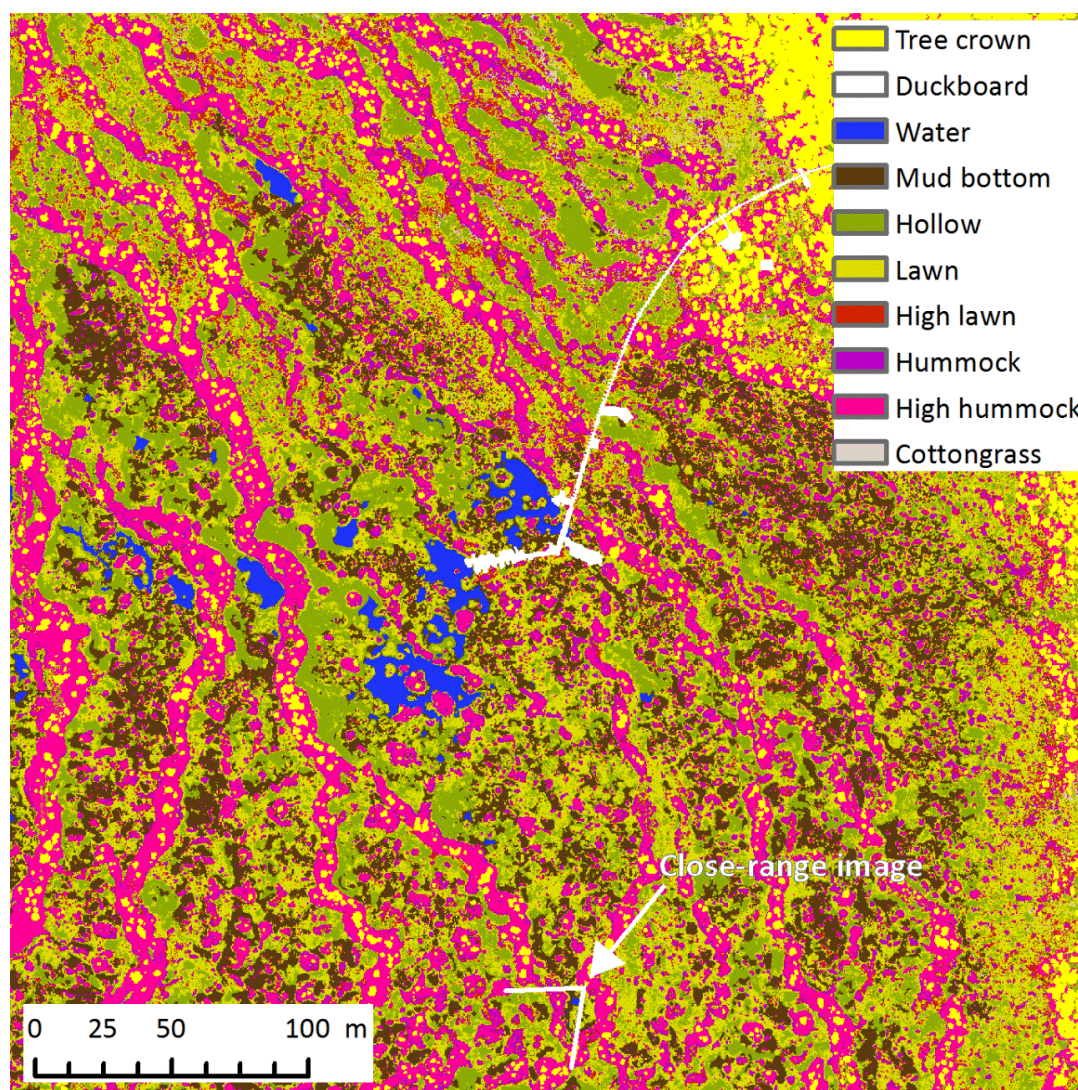


Figure 14. RF-classified map of the AOI. The field-of-view of the close-range image shown in Figures 7 and 16 is marked in the south.

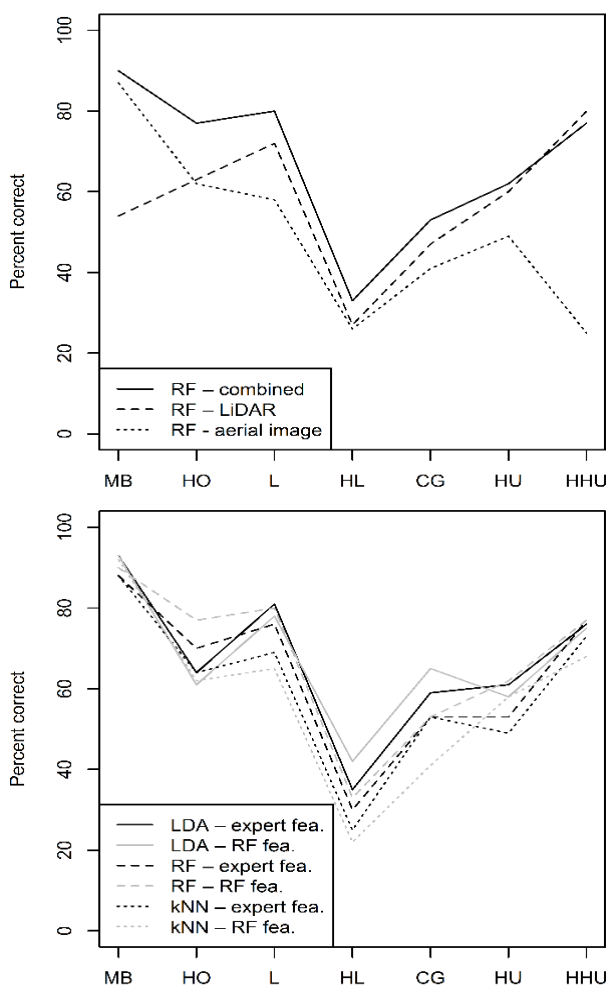


Figure 15. Class-by-class classification accuracy by using (a) the RF algorithm and RF variables and (b) the combined features in two feature sets and three classifiers.

Table 10. Best-case LDA classification performance with the combined (top row), image-based (middle row) and LiDAR-based (bottom row) expert features. Leave-one-out CV.

	MB	HO	L	HL	CG	HU	HHU	Total	Acc
	<b>77</b>	1	5					83	93
MB	<b>72</b>	1			4		6	83	87
	<b>32</b>	43	8					83	39
	7	<b>108</b>	50		2	2		169	64
HO	6	<b>98</b>	57		1	2	5	169	58
	7	<b>93</b>	66		1	2		169	55
	3	21	<b>167</b>	10	3	1		205	81
L	2	29	<b>129</b>	7	3	18	17	205	63
	6	33	<b>155</b>	6	1	4		205	76
		2	23	<b>31</b>	5	28		89	35
HL	1	5	16	<b>22</b>	6	34	5	89	25
	3	3	32	<b>19</b>	5	27		89	21
	1		3		<b>10</b>	3		17	59
CG	1		2		<b>12</b>	1	1	17	71
	1		3		<b>9</b>	3	1	17	53
	1	2	9	18	7	<b>72</b>	9	118	61
HU	4	3	22	21	9	<b>53</b>	6	118	45
	2		22	6	8	<b>67</b>	13	118	57
			1		6	11	<b>57</b>	75	76
HHU	8	4	24	2	6	12	<b>19</b>	75	25
	1				4	13	<b>57</b>	75	76

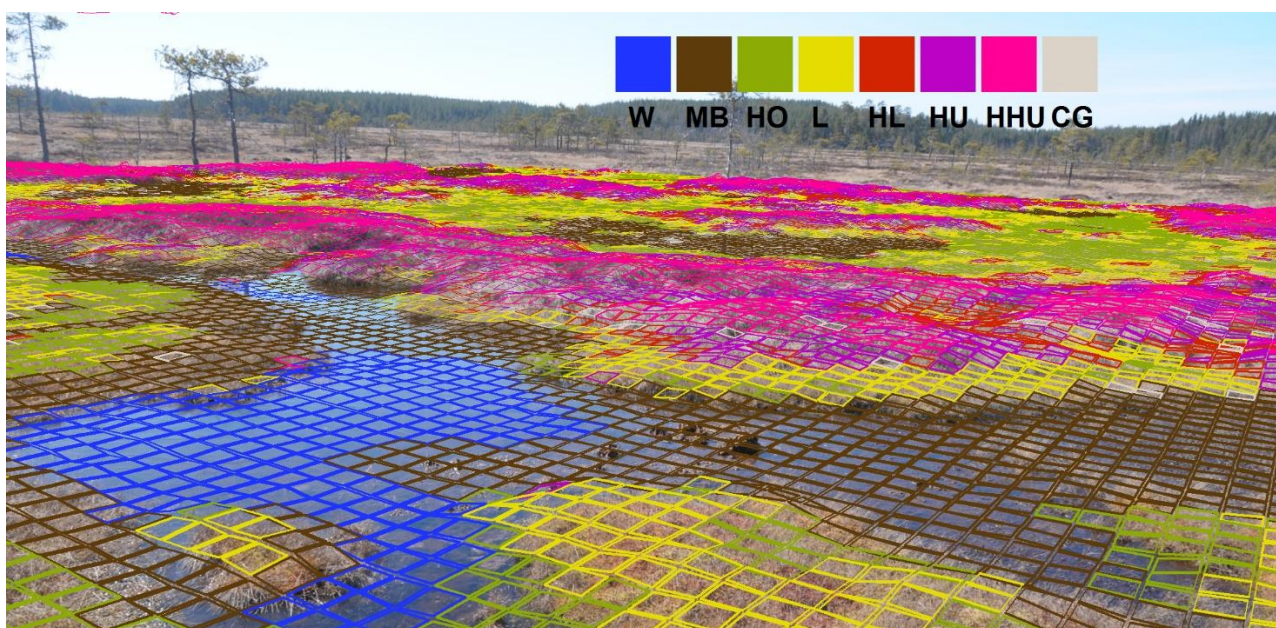


Figure 16. Visualisation of the resulting LDA-classified raster map with 20 × 20-cm cells. The location is shown in Figure 14.

## DISCUSSION

We demonstrated the co-use of passive imaging and WF-recording LiDAR for the classification of oligo-ombrotrophic bog vegetation in a 16-hectare area, where water and mud-bottom hollows had a joint coverage of about 20 %, while *Sphagnum* mosses prevailed on the other surface types. The microforms were high hummock (HHU), hummock (HU), high lawn (HL), lawn (L), hollow (HO), mud-bottom (MB), water (W) and cottongrass (CG). The topography of the bog was specific as the surface

Table 11. Comparison of classification results (%) within a radius of 150 m from the EC tower. The standard error estimates in percentage points are given in parentheses for the 2012 (systematic cluster-based) field inventory and are based on the random sampling assumption.

Class	RF	LDA	Field
W	2.3	2.3	2.0 (0.9)
MB	15.9	17.2	15.8 (2.0)
HO	19.9	14.2	19.2 (2.4)
L	26.9	29.5	18.2 (2.2)
HL	7.2	5.0	12.8 (1.8)
CG	0.6	5.3	- (-)
HU	11.0	10.9	10.8 (1.6)
HHU	16.2	15.6	21.2 (2.5)

elevation and water level increased in steps between long hummocks (ridges) that had a separation of 25–100 m. The target classes were specified by ecologists, and while the botanical descriptions were rather unambiguous, the DCA analyses and experience in the field gave support to the anticipation of large within-class variation as well as between-class overlap. Thus, very high (>90 %) classification accuracy could not be expected.

High ground sampling density LiDAR echoes captured the local elevation variation at an RMS-accuracy of about 3 cm, which enabled the detection of hummocks, hollows and intermediate surfaces. Waveform data were useful in detecting trees and echo width was specific to two target classes with taller field layers. As expected, LiDAR intensity at 1550 nm was associated with wetness.

The colours of the aerial RGB images could be linked with the colouring of the various *Sphagnum* species. Ten different *Sphagnum* species were identified in the field. However, as it is known that their colours vary with moisture content and light exposure and are not distinctive features, RGB image features were not particularly strong predictors.

We analysed directional anisotropy, which is influenced by the reflectance properties of the objects and which affects image observations made in varying view-illumination geometry. This variation is always present even in a single frame image and needs to be accounted for when multiple images of the same target are acquired. The findings implied that class-specific differences exist, and they hinder the use of a single BRDF-correction to correct for anisotropy induced imbalances in multi-image data.

Table 12. Neighbourhood relations between classes (%). For example, 36.7 % of the 3×3-neighbourhood pixels of high lawn (HL) pixels belong to the same class, while 23 % belong to hummock (HU). DB = white wooden duckboard (see Figure 14; manually delineated). All cells are non-zero.

	MB	HO	L	HL	CG	HU	HHU	Tree	W	DB
MB	82.5	5.4	8.6	1.3	0.1	1.4	0.3	0.1	0.3	0.0
HO	3.9	<u>71.9</u>	21.7	0.8	0.2	0.4	0.5	0.5	0.1	0.0
L	4.3	15.2	<u>66.3</u>	7.9	0.9	4.4	0.7	0.3	0.0	0.0
HL	2.5	2.2	30.0	<u>36.7</u>	2.0	23.0	3.1	0.4	0.0	0.1
CG	2.1	5.6	30.0	18.4	<u>27.3</u>	13.6	2.1	0.9	0.0	0.1
HU	1.8	0.7	11.5	15.7	1.0	<u>54.8</u>	14.0	0.5	0.0	0.0
HHU	0.3	0.7	1.3	1.5	0.1	10.0	<u>81.6</u>	4.5	0.0	0.0
Tree	0.1	0.7	0.5	0.2	0.0	0.4	4.7	<u>93.4</u>	0.0	0.0
W	3.3	1.6	0.9	0.1	0.0	0.1	0.1	0.0	<u>93.8</u>	0.1
DB	1.0	1.4	2.4	1.1	0.1	0.8	0.8	1.6	0.3	<u>90.5</u>

The classification trials confirmed this, when nadir-corrected image features were outperformed by simple averaged values. The wide-band RGB-sensor data did not show spectral differences in anisotropy, although it was expected that the BLU band would show lesser effects due to diffuse solar illumination. Analyses of variance using mixed-effects modelling revealed a strong target effect, i.e. the field sample deviated consistently in all views and the residual error, that cancels out when multiple image observations are weighted for a mean value, was small. A large part of the feature variance is explained by the target itself. This effect explains why additional image observations do not usually improve the classification performance significantly (e.g. Packalén *et al.* 2009, Korpela *et al.* 2014, cf. Jääskeläinen *et al.* 1994). We could show between-class differences in anisotropy that were linked to the presence and type of field layer. Directional anisotropy explained from 4 to 30 % of feature variance and the surfaces varied in how the signal changed away from the nadir towards the back- and forward-scatter geometries.

Our method aimed to produce a raster map at a resolution of 20 cm. All predictors were represented by raster models in the same grid. The LiDAR, image and field data were accurately co-registered, which is a necessity. However, it is advisable to use 3D monuments and signals in the field to assure co-registration, as the use of natural targets (which we needed to resort to) is less accurate. We used topographic and image texture to assess the match between LiDAR/image and field GNSS data. As we had no signals in the field, the exterior orientation of both the images and LiDAR relied on direct sensor orientation which, unless the sensors are accurately calibrated, introduces a risk of systematic geometric errors. In our data, the camera calibration had an error in the camera constant that caused the photogrammetric image block to be systematically off by 30 cm. In addition, the original automatic aerial triangulation had resulted in an image block with few tie points between flight lines. Motion blur in the images had possibly contributed to this outcome. It is evident that LiDAR could have been replaced by photogrammetry in reconstructing the geometry of the bog surface, by utilising low-altitude imaging and UAVs. However, in that case LiDAR intensity and the waveforms traits would be absent and the detection of trees would have been challenging as the crowns were sparse and poorly visible in the images.

The echo width measurement in the LMS-Q680i sensor was influenced by signal strength. The observed 0.6-ns or 9-cm system-induced trend would

typically be neglected in e.g. forest canopies, but the trend could not be overlooked in analysing the 0–30-cm-high field layer vegetation. Similar findings concerning the limited bandwidth characteristics of WF-recording sensors are presented by Korpela (2017), who reported small differences between the echo width of weak and strong signals in the Leica ALS60 sensor. Normalising the non-linear amplitude scale enabled accurate observations of surface roughness within the footprint, and, as expected, echo width was larger in hummock and cottongrass vegetation. Factory calibration of the sensor was applied by the data provider and the discrete-return intensity data were on the ratio scale, which enabled the use of the radar equation to carry out range normalisation. If the intensity data are not on the ratio scale, the correction using the radar equation worsens data quality (Korpela *et al.* 2010).

The DEM and intensity features were good LiDAR predictors. Both LiDAR and aerial image-based features were needed for best-case classification performance. In general, LiDAR features were superior. However, cottongrass separated well in the images, which is in accordance with the findings of Kalacska *et al.* (2013).

Lehmann *et al.* (2016) employed a UAV equipped with a modified colour-infrared camera for classifying microtopography on a hummocky (valley) bog in Patagonia and obtained impressive results, with an OA of 86 % ( $\kappa$  of 0.83). They had five classes, one of which was water (whereas we had eight surface types). Cell size was 60 cm and the reference data were collected by visual interpretation of the same images that were used in the analyses, which may have influenced the validity of the reported performance metrics. We did not try different sensors or acquisition settings. It is likely that LiDAR features will be blurred at lower pulse densities or by larger footprints. We considered additional imaging by UAVs, but the relatively large area and the remote location set the costs too high. UAV photogrammetry, if it replaces the LiDAR data in 3D modelling, will require a dense network of elevation control. While manned platforms are efficient, low-altitude photogrammetry combined with field surveying may well be a viable option in smaller areas. However, improving the DEM accuracy from the 2–3-cm level will be challenging using imagery without excessive efforts in the field, as exceedingly accurate direct georeferencing (GNSS-aided inertial navigation) is currently expensive for UAVs.

We tested three classifiers. The kNN-method was outperformed by LDA and RF, as was also reported for mire habitat classification (Korpela *et al.* 2009).

We applied pixel-based classification and omitted spatial dependencies as we had no exact data about the neighbourhood connections. For example, Haapanen & Tokola (2007) employed the sequential maximum a posteriori (SMAP) classification to Landsat TM data and reported improved mire habitat classification results with SMAP compared to ordinary maximum likelihood. Conditional random fields are state-of-the-art methods that can be used for contextual labelling of scene points such that spatial dependencies are considered (e.g. Niemeyer *et al.* 2013). However, the neighbourhood relations of microforms are complex compared to rules that can be applied in labelling targets in, for example, urban environments.

The classification accuracies obtained were reasonable, considering the 'botanical overlap' of some classes. However, an accuracy below 80 % does not provide a very reliable basis for directly observing subtle microform changes at the distribution level. Comparisons and GIS-analyses of the current DEM and image features with future data will be more interesting when all multi-temporal data are accurately co-registered. It is worth noting that we delineated the pools manually. In many cases there were no LiDAR data from water and the pools showed as dark surfaces in the images, except for occasional sun glints. The labelling in the map was topologically sound with e.g. water being neighboured by mud-bottom hollow, hollow or lawn. Unfortunately, we have not yet been able to complete our (ongoing) evaluation of the map's utility for up-scaling greenhouse gas flux measurements and/or estimating the footprint of the EC tower.

Our LiDAR sensor was a single-band device that operated at 1550 nm. This wavelength is more efficient for detecting wetness differences than the other commonly available wavelengths of 1064 and 532 nm. The low flying resulted in narrow footprint data, which is beneficial for elevation modelling, as the elevation represents a weighted average of the footprint. Similarly, the backscattering occurred from a small area for which the coordinates were accurate. Multi-band LiDAR sensors are entering the market and constitute an interesting future option for data acquisition. Advances in the receiver design (sensitivity improvements) of pulsed LiDAR sensors are also anticipated (photon-counting). These techniques may help in detecting trees (weak backscattering) and the shrub-layer.

The RGB camera with the Bayes-filter is not comparable with state-of-the-art photogrammetric sensors which have narrower bands, small pixels, radiometric calibration and stable geometry, and which enable multi-view analyses. Hyperspectral

sensors would provide more radiometric information but that usually comes at a cost, i.e. with larger pixels and monoscopic data. On the other hand, their one-dimensional view geometry is favourable as it simplifies the modelling of directional effects (Schaepman-Strub *et al.* 2006, Korpela *et al.* 2011, Koukal & Atzberger 2012).

The airborne data were acquired in early summer, which may have been suboptimal, as there were very few green field-layer plants. On the other hand, the *Sphagnum* mosses, with more distinguishable colours than vascular plants, were well visible.

The maps, field samples and LiDAR data are interesting sources of information for long term monitoring of the site. The cost of such data is 0.05–0.25 € m<sup>-2</sup> depending mainly on the size of the area and the number of airborne acquisitions. In Finland, the GNSS infrastructure is excellent, which is not self-evident in many parts of the world. Our AOI was a sparsely forested ombrotrophic bog. We also see potential in using the methodology in fen vegetation, where the WF LiDAR data can find wet microforms and capture the relatively low topographic variation, and the echo width may help in differentiating sedge stands of varying species, size and density.

## CONCLUSIONS

Based on the results we conclude:

- Fusion of airborne LiDAR and images is well suited for sparsely forested and open bogs, as the shading and occlusion by trees has a lesser effect.
- High-density LiDAR captures the topographic variations in the resulting elevation model and DEM features are efficient predictors of the microforms.
- WF data help in finding trees that are hardly discernible in images owing to their sparse foliage. WF can be used to constrain the LiDAR data to 'radiometrically intact' pulses that contain full energy at the bog surface, which makes intensity data more reliable.
- Echo width feature responded to surface roughness and dense field layer vegetation.
- Shortwave-infrared LiDAR intensity varied from no-data in water to strong echoes in the hummock vegetation and constitutes a good predictor of surface wetness.

Directional reflectance anisotropy depended on the surface type and especially on the presence of shrubs

and other field layer vegetation that contribute to shadow casting. It probably will be possible to slightly enhance the classification results obtained by using microform- and band-specific ‘anisotropy prototypes’ which are contrasted against the observations in multiple images.

The 3D fusion of LiDAR and image data employed here comprises a promising approach, which can be developed further by using radiometrically more advanced imaging sensors, along with more careful data acquisition in which aspects such as image motion blur, geometric control and objective sampling of the field data are considered.

## ACKNOWLEDGEMENTS

We thank the Finnish Geodetic Institute for providing the GNSS equipment in April 2014 as well as Dr Andreas Roncat, who kindly gave us his MATLAB interface to the proprietary LiDAR observations files. We acknowledge Dr Ben Clutterbuck and the other (anonymous) reviewers for their important remarks. The research (IK and RH) was funded by the Academy of Finland.

## AUTHOR CONTRIBUTIONS

TV, EST and IK arranged the LiDAR acquisition in May 2013 and conceived the original idea. AK and IK did the vegetation survey in April 2014. EST provided data from the 2012–13 vegetation surveys and conducted the ordination analyses. IK developed and implemented the remote sensing method, planned the experiments with AK, wrote the manuscript together with RH, and supervised RH who implemented the GIS-analyses and classification tasks. All authors contributed to the final version of the manuscript.

## REFERENCES

- Ahokas, E., Kaasalainen, S., Hyyppä, J., Suomalainen, J. (2006) Calibration of the Optech ALTM 3100 laser scanner intensity data using brightness targets. *Revue Française de Photogrammétrie et de Télédétection*, 182(2), 10–16.
- Breiman, L. (2001) Random forests. *Machine Learning*, 45(1), 5–32.
- Doneus, M., Briese, C., Fera, M., Janner, M. (2008) Archaeological prospection of forested areas using full-waveform airborne laser scanning. *Journal of Archaeological Science*, 35(4), 882–893.
- Frolking, S., Roulet, N.T. (2007) Holocene radiative forcing impact of northern peatland carbon accumulation and methane emissions. *Global Change Biology*, 13(5), 1079–1088.
- Gallego-Sala, A.V., Charman, D.J., Brewer, S., Page, S.E. and 71 others (2018) Latitudinal limits to the predicted increase of the peatland carbon sink with warming. *Nature Climate Change*, 8, 907–913.
- Gatziolis, D. (2011) Dynamic range-based intensity normalization for airborne, discrete return LiDAR data for forest canopies. *Photogrammetric Engineering & Remote Sensing*, 77(3), 251–259.
- Gorham, E. (1991) Northern peatlands: Role in the carbon cycle and probable responses to climatic warming. *Ecological Applications*, 1(2), 182–195.
- GRASS Development Team (2015) *Geographic Resources Analysis Support System (GRASS) Software*, Version 6.4.5. Open Source Geospatial Foundation. Online at: <http://grass.osgeo.org>
- Haapanen, R., Tokola, T. (2007) Creating a digital treeless peatland map using satellite image interpretation. *Scandinavian Journal of Forest Research*, 22(1), 48–59.
- Hämet-Ahti, L., Suominen, J., Ulvinen, T., Uotila, P. (1998) *Retkeilykasvio (Field Flora of Finland)*. Luonnontieteellinen keskusmuseo, Kasvimuseo, Helsinki, 656 pp. (in Finnish).
- Hassel, K., Kyrkjeeide, M.O., Yousefi, N., Prestø, T., Stenøien, H.K., Shaw, J.A., Flatberg, K.I. (2018) *Sphagnum divinum* (sp.nov.) and *S. medium* Limpr. and their relationship to *S. magellanicum* Brid. *Journal of Bryology*, 40(3), 197–222.
- Hastie, T., Tibshirani, R., Friedman, J. (2001) *The elements of statistical learning: data mining, inference and prediction*. Springer-Verlag, New York, 552 pp.
- Höfle, B., Pfeifer, N. (2007) Correction of laser scanning intensity data: data and model-driven approaches. *ISPRS Journal of Photogrammetry & Remote Sensing*, 62(6), 415–433.
- Ise, T., Dunn, A.L., Wofsy, S.C., Moorcroft, P.R. (2008) High sensitivity of peat decomposition to climate change through water-table feedback, *Nature Geoscience*, 1(11), 763–766.
- Jääskeläinen T., Silvennoinen R., Hiltunen J., Parkkinen J. (1994) Classification of the reflectance spectra of pine, spruce, and birch. *Applied Optics*, 33(12), 2356–2362.
- Jutzi, B., Gross, H. (2009) Normalization of LiDAR intensity data based on range and surface incidence angle. *International Archives of*

- Photogrammetry, Remote Sensing and Spatial Information Sciences*, 38, 213–218.
- Kaasalainen, S., Jaakkola, A., Kaasalainen, M., Krooks, A., Kukko, A. (2011) Analysis of incidence angle and distance effects on terrestrial laser scanner intensity: Search for correction methods. *Remote Sensing*, 3(10), 2207–2221.
- Kalacska, M., Arroyo-Mora, J.P., de Gea, J., Snirer, E., Herzog, C., Moore, T.R. (2013) Videographic analysis of *Eriophorum vaginatum* spatial coverage in an ombrotrophic bog. *Remote Sensing*, 5(12), 6501–6512.
- Korpela, I. (2008) Mapping of understory lichens with airborne discrete-return LiDAR data. *Remote Sensing of Environment*, 112(10), 3891–3897.
- Korpela, I. (2017) Acquisition and evaluation of radiometrically comparable multi-footprint airborne LiDAR data for forest remote sensing. *Remote Sensing of Environment*, 194, 414–423.
- Korpela, I., Koskinen, M., Vasander, H., Holopainen, M., Minkkinen, K. (2009) Airborne small-footprint discrete-return LiDAR data in the assessment of boreal mire surface patterns, vegetation, and habitats. *Forest Ecology and Management*, 258(7), 1549–1566.
- Korpela, I., Ørka, H.O., Heikkinen, V., Tokola, T., Hyypä, J. (2010) Range- and AGC normalization of LiDAR intensity data for vegetation classification. *ISPRS Journal of Photogrammetry and Remote Sensing*, 65(4), 369–379.
- Korpela, I., Heikkinen, V., Honkavaara, E., Rohrbach, F., Tokola, T. (2011) Variation and directional anisotropy of reflectance at the crown scale – Implications for tree species classification in digital aerial images. *Remote Sensing of Environment*, 115(8), 2062–2074.
- Korpela, I., Mehtätalo, L., Markelin, L., Seppänen, A., Kangas, A. (2014) Tree species identification in aerial image data using directional reflectance signatures. *Silva Fennica*, 48(3), 1–20.
- Koukal, T., Atzberger, C. (2012) Potential of multi-angular data derived from a digital aerial frame camera for forest classification. *IEEE Journal of Selected Topics in Applied Earth Observations and Remote Sensing*, 5(1), 30–43.
- Laine, A.M., Byrne, K.A., Kiely, G., Tuittila, E-S. (2007a) Patterns in vegetation and CO<sub>2</sub> dynamics along a water level gradient in a lowland blanket bog. *Ecosystems*, 10(6), 890–905.
- Laine, A.M., Wilson, D., Kiely, G., Byrne, K.A. (2007b) Methane flux dynamics in an Irish lowland blanket bog. *Plant and Soil*, 299(1), 181–193.
- Laine, J., Harju, P., Timonen, T., Laine, A., Tuittila, E-S., Minkkinen, K., Vasander, H. (2011) *The Intricate Beauty of Sphagnum Mosses – A Finnish Guide to Identification*. Second amended edition, University of Helsinki Department of Forest Sciences Publications 2, 191 pp.
- Laine, J., Sallantausta, T., Syrjänen, K., Vasander, H. (2016) *Sammalten kirjo (The Spectrum of Mosses)*. Metsäkustannus, Helsinki, 208 pp. (in Finnish).
- Lehmann, J.R.K., Münchberger, W., Knoth, C., Blodau, C., Nieberding, F., Prinz, T., Pancotto, V.A., Kleinebecker, T. (2016) High-resolution classification of South Patagonian peat bog microforms reveals potential gaps in up-scaled CH<sub>4</sub> fluxes by use of Unmanned Aerial System (UAS) and CIR Imagery. *Remote Sensing*, 8(3), 1–19.
- Liaw, A., Wiener, M. (2002) Classification and regression by randomForest. *R News*, 2(3), 18–22. Online at: [https://cran.r-project.org/doc/Rnews/Rnews\\_2002-3.pdf](https://cran.r-project.org/doc/Rnews/Rnews_2002-3.pdf), accessed 11 Feb 2020.
- Maanavilja, L., Riutta, T., Aurela, M., Pulkkinen, M., Laurila, T., Tuittila, E.-S. (2011) Spatial variation in CO<sub>2</sub> exchange at a northern aapa mire. *Biogeochemistry*, 104(1), 325–345.
- Mathijssen, P., Väiliranta, M., Korrensalo, A., Alekseychik, P., Vesala, T., Rinne, J., Tuittila, E.-S. (2016) Reconstruction of Holocene carbon dynamics in a large boreal peatland complex, southern Finland. *Quaternary Science Reviews*, 142, 1–15.
- Millard, K., Richardson, M. (2013) Wetland mapping with LiDAR derivatives, SAR polarimetric decompositions, and LiDAR–SAR fusion using a random forest classifier. *Canadian Journal of Remote Sensing*, 39(4), 290–307.
- Morin, T.H., Bohrer, G., Stefanik, K.C., Rey-Sanchez, A.C., Matheny, A.M., Mitsch, W.J. (2017) Combining eddy-covariance and chamber measurements to determine the methane budget from a small, heterogeneous urban floodplain wetland park. *Agricultural and Forest Meteorology*, 237–238, 160–170.
- Niemeyer, J., Rottensteiner, F., Soergel, U. (2013) Classification of urban LiDAR data using conditional random field and random forests. In: *Proceedings of the Joint Urban Remote Sensing Event (JURSE) 2013* (Sao Paulo, Brazil), IEEE, 139–142. Online at: <https://ieeexplore.ieee.org/document/6550685>, accessed 11 Feb 2020.
- Packalén, P., Suvanto, A., Maltamo, M. (2009) A two stage method to estimate species-specific growing stock. *Photogrammetric Engineering & Remote Sensing*, 75(12), 1451–1460.
- Poulin, M., Careau, D., Rochefort, L., Desrochers, A. (2002) From satellite imagery to peatland vegetation diversity: How reliable are habitat

- maps? *Conservation Ecology*, 6(2), 16, 31 pp.
- Quantum GIS Development Team (2015) *QGIS Geographic Information System*. Open Source Geospatial Foundation Project. Online at: <http://www.qgis.org/>
- Rapinel, S., Hubert-Moy, L., Clément, B. (2015) Combined use of LiDAR data and multispectral earth observation imagery for wetland habitat mapping. *International Journal of Applied Earth Observation and Geoinformation*, 37, 56–64.
- Riutta, T., Laine, J., Aurela, M., Rinne, J., Vesala, T., Laurila, T., Haapanala, S., Pihlatie, M., Tuittila, E.-S. (2007) Spatial variation in plant community functions regulates carbon gas dynamics even in a seemingly homogenous boreal fen ecosystem. *Tellus*, 59B, 838–852.
- Schaepman-Strub, G., Schaepman, M.E, Painter, T.H, Dangel, S., Martonchik, J.V. (2006) Reflectance quantities in optical remote sensing – definitions and case studies. *Remote Sensing of Environment*, 103(1), 27–42.
- Strack, M. (ed.) (2008) *Peatlands and Climate Change*. International Peatland Society, Jyväskylä, Finland, 223 pp.
- ter Braak, C.J.F., Šmilauer, P. (2012) *Canoco Reference Manual and User's Guide: Software for Ordination, Version 5.0*. Microcomputer Power, Ithaca, USA, 496 pp.
- Wagner, W., Roncat, A., Melzer, T., Ullrich, A. (2007) Waveform analysis techniques in airborne laser scanning. *International Archives of Photogrammetry, Remote Sensing and Spatial Information Sciences*, 36(3/W52), 413–418.
- Väliranta, M., Korhola, A., Seppä, K., Tuittila, E.S., Sarmaja-Korjonen, K., Laine, J., Alm, J. (2007) High-resolution reconstruction of wetness dynamics in a southern boreal raised bog, Finland, during the late Holocene: a quantitative approach. *The Holocene*, 17(8), 1093–1107.
- Vasander, H., Laine, J. (2008) Classification of peatlands drained for forestry. In: Korhonen, R., Korpela, L., Sarkkola, S. (eds.) *Finland - Fenland*. Finnish Peatland Society, Helsinki, 146–151.
- Submitted 21 Nov 2018, revision 19 Dec 2019  
Editor: Olivia Bragg

---

Author for correspondence:

Dr Ilkka Korpela, Department of Forest Sciences, University of Helsinki, P.O. Box 27, 00014, Finland.  
Tel: +358-400-218305; E-mail: [ilkka.korpela@helsinki.fi](mailto:ilkka.korpela@helsinki.fi)